

# Investigating the relation between Star Formation and Environment at $z \sim 1$ Using the ORELSE Survey

Finn Giddings<sup>a</sup>, Roy Gal<sup>b</sup>, Brian Lemaux<sup>c</sup>, Adam Tomczak<sup>c</sup>, Lori Lubin<sup>c</sup>, Denise Hung<sup>b</sup>, Priti Staab<sup>c</sup>, Lu Shen<sup>c</sup>

<sup>a</sup>*Rhodes College, 2000 North Pkwy, Memphis, TN 38112*

<sup>b</sup>*Institute for Astronomy, University of Hawai'i, 2680 Woodlawn Drive, Honolulu, HI 96822, USA*

<sup>c</sup>*University of California, Davis, 1 Shields Ave, Davis, CA 95616*

---

## Abstract

We present a study on the relationship between star formation rate (SFR) and environmental overdensity in galaxy clusters around redshift  $z \sim 1$  using galaxy cluster samples drawn from the Observations of Redshift Evolution in Large-Scale Environments (ORELSE) Survey. With data from the 15 fields of the ORELSE survey, we examine the dependence of two different star formation indicators,  $[\text{O II}] \lambda 3727 \text{ \AA}$  and UV+IR emission, on two different overdensity indicators,  $\log(1 + \delta_{\text{gal}})$  (local overdensity) and  $\log(\eta)$  (distance from the cluster center). We bin our sample by cluster redshift and cluster mass along with galaxy mass to investigate the impact of environment on star formation. We find that intermediate-mass galaxies ( $10.1 \leq \log(M_*/M_\odot) \leq 10.8$ ) at higher redshifts and in more dense environments exhibit both higher SFRs and higher SFR efficiency (on average  $\sim 0.5\sigma$  in the log for both) relative to field galaxies, as well as to similar mass galaxies at lower redshift (by a factor of 2 in the log and by an order of magnitude respectively). High-mass galaxies ( $\log(M_*/M_\odot) \geq 10.8$ ) in our higher redshift bins also experience little suppression, but are only comparable to the corresponding field galaxies rather than enhanced. Galaxies in clusters in our lower redshift sample have suppressed SFR relative to field galaxies (as is the case locally), but at higher redshift we do not see this trend. We also observe a population of high- and intermediate-mass galaxies in the highest density environments at high redshift, with high star formation rates, which have not been previously seen. We dub these “4H” galaxies and examine their properties for clues to their origin.

*Keywords:* galaxies – environment, galaxies – star formation, galaxies – clusters

---

---

*Email address:* `gidfd-22@rhodes.edu` (Finn Giddings)

## 1. Introduction

The connection between star formation and environment in galaxy groups and clusters plays a fundamental role in the high-mass large-scale structure of the universe. In the local Universe, this relationship between star formation and environment is well understood, with, on average, galaxies in regions of higher overdensity having lower star-formation rates (SFRs) than when compared to galaxies located in regions of lower overdensity (Lewis et al., 2002; Gómez et al., 2003; Christlein and Zabludoff, 2005; Cooper et al., 2008; Tomczak et al., 2019). At these lower redshifts, galaxies within clusters are suppressed of their star formation relative to the surrounding field, and this effect is heightened in more dense environments (Rasmussen et al., 2012). As studies have expanded farther into the universe and to higher redshifts, the impact of environment on star formation is less well studied, and thus less understood. At  $z > 1.5$ , many studies show high levels of star formation in the cores of clusters, thus signaling a change in the relation between density and star formation (Tran et al., 2010; Strazzullo et al., 2013; Santos et al., 2015; Wang et al., 2016; Noirod et al., 2018). Yet, many of these studies are restricted to the centers of the clusters, and do not consider galaxies in the nearby field. Additionally, the epoch of this change remains elusive: with many studies in  $0.5 < z < 1.5$  giving mixed results. Some find that within this redshift range the star formation-density relation is reversed with regions of higher density having higher SFR (Elbaz et al., 2007; Cooper et al., 2008; Popesso et al., 2011), but others find that with clusters within this range there is no significant change in the SFR-density relation (Patel et al., 2011; Muzzin et al., 2012; Ziparo et al., 2014). There are even studies that find star formation to be largely independent of environment within this redshift range (Grützbauch et al., 2011; Darvish et al., 2016). Much of the tension among these findings can be attributed to the fact that there is no common way to calculate a galaxies environment, nor a single procedure for revealing the indicators of SFR (e.g., spectral energy distribution (SED) fitting vs, [O II]  $\lambda$  3727 Å emission vs, etc.), and the fact that contamination by active galactic nuclei (AGN) can also impact and muddle results.

Galaxy clusters and superclusters represent much of the Universe's large-scale structure and to understand them one must shed light on what causes the current arrangement of galaxy clusters, the physical properties they have, and how those properties correlate to one another, as well as the trends in characteristics of their corresponding member galaxies. Surveys at extremely low redshift, along with various numerical simulations, unveil a filamentary structure within the universe that stretches between galaxy clusters and superclusters (Geller and Huchra, 1989; Einasto et al., 1997; Colberg et al., 2000; Colless et al., 2001; Evrard et al., 2002; Dolag, 2006). At nodes of this filamentary structure, clusters form through accreting galaxies and groups of galaxies from the surrounding field (Frenk et al., 1996; Eke et al., 1998). Through this mode, galaxies begin to slowly group together, thus affecting their own individual properties and combining to create the characteristics of the larger cluster.

On the individual galaxy level, the environment in which it resides – which is oftentimes intimately tied to its relation to a cluster – plays a significant role in its evolution and in its physical qualities (Muzzin et al., 2012, 2014; Balogh et al., 2016; Tomczak et al., 2017,

2019; Lemaux et al., 2017, 2019). For example, galaxies in regions of higher density have an elliptical morphology more frequently (Dressler, 1980), and tend to have older stellar populations (Smith et al., 2006; Cooper et al., 2008). These galaxies also exhibit redder colors and higher stellar masses (Hogg et al., 2004; Kauffmann et al., 2004). This is, in part, due to various physical processes, such as ram-pressure stripping (Gunn and Gott, 1972; Hester, 2006; Boselli et al., 2009) or galaxy harassment (Moore et al., 1996, 1998), that rapidly remove gas from the galaxies as they begin to fall into larger groups and clusters (i.e. regions of higher density). These higher density processes often help to quench galaxies of star forming material, and lead to a depletion of star formation within them as the galaxies are starved of essential star forming gas. This star forming gas is oftentimes in the form of neutral hydrogen ( $H_2$ ) and atomic neutral hydrogen (HI), and the depletion of a galaxies hydrogen reservoirs directly regulates its star formation abilities (Guo et al., 2021).

The Observations of Redshift Evolution in Large-Scale Environments (ORELSE) Survey is a study of large-scale structure (LSS) that contains data concerning many of these key parameters. The ORELSE survey primarily focuses on structure at scales greater than  $10 h_{70}^{-1}$  Mpc around 20 well-known clusters at redshifts  $0.6 < z < 1.3$ , and contains an unprecedented amount of spectroscopic coverage with hundreds to thousands of high-quality spectra and redshifts per field (Lubin et al., 2009). The survey covers 5 square degrees, all targeted at intermediate-to-high-density regions, making it complementary and comparable to field surveys such as the Deep Extragalactic Evolutionary Probe 2 Redshift Survey (DEEP2; Davis et al. (2003)) and the Cosmological Evolution Survey (COSMOS; Scoville et al. (2007); Koekemoer et al. (2007)). The ORELSE survey has been the source for a number of subsequent studies, and has been expanded on by the work of Hung et al. (2020). In this study, we will utilize data from the expanded Hung et al. (2020) where possible, so, for brevity, any mention to ORELSE data implies this data as well.

In this paper, we leverage galaxy data samples drawn from the ORELSE survey to investigate the relation between star formation rate and environment around  $z \sim 1$ . In Section 2, we discuss the data and sample selection along with the various processes – including Voronoi tessellation Monte Carlo (VMC) mapping – used to filter and obtain the measurements. Section 3 contains our main findings regarding star formation and overdensity, while Section 4 explores the significance and implication of these findings. Throughout the paper, we use a cosmology with  $H_0 = 70 h_{70}^{-1} \text{ km s}^{-1} \text{ Mpc}^{-1}$ ,  $\Omega_m = 0.3$ , and  $\Omega_\Lambda = 0.7$ .

## 2. Data and Methods

### 2.1. The ORELSE Survey

This paper utilizes data from the ORELSE Survey (Lubin et al., 2009). The ORELSE cluster sample is drawn from various other surveys that employ a variety of different detection techniques (X-ray, radio, optical) to reduce any bias within the sample selection (Oke et al., 1998; Rosati et al., 1998; Vikhlinin et al., 1998; Gladders and Yee, 2005; Gioia et al., 1999, 2003; Stanford et al., 2002; Blanton et al., 2003; Hashimoto et al., 2005; Henry et al., 2006;

Pierre et al., 2006; Maughan et al., 2006). The ORELSE survey’s first detected large scale structure was the CL 1604 supercluster and it has the most extensive multi-wavelength photometric and multi-object spectroscopic data (see Gal et al., 2008). The properties of the confirmed members of CL 1604 are used as a guide throughout the ORELSE survey for choosing appropriate galaxy magnitude and color selections in the other clusters (Lubin et al., 2009).

The first phase of the ORELSE survey was to do wide-field (25’) optical/near-infrared (r’ i’ z’ Ks) imaging of the 20 cluster fields with all of the near-infrared observations being original to the ORELSE survey, and the optical imaging coming from both new and archived observations (see Table 1 of Lubin et al. (2009)). The ORELSE survey employed the Large Format Camera (LFC; Simcoe et al. (2000)) and the Wide-Field Infrared Camera (WIRC) on the Palomar 5 m, Suprime-Cam on the Subaru 8 m (Miyazaki et al., 2002), the Wide-Field Infrared Camera (WFCAM) on the United Kingdom Infra-Red Telescope (UKIRT) 3.8 m, and the Florida Multi-Object Imaging Near IR Grism Observational Spectrometer (FLAMINGOS) on the Kitt Peak National Observatory (KPNO) 4 m in their original observations to cover an area of at least  $0.2 \text{ deg}^2$  around each of the 20 target clusters (Lubin et al., 2009). For the XLSS005 field, the initial optical imaging was acquired with MegaCAM (Boulade et al., 2003). This original optical imaging was initially used to characterize the large-scale environment around the target clusters, as well as to identify possible cluster members for follow up multi-object spectroscopy, and the near-infrared Ks imaging was used to measure stellar masses and provide improved photometric redshifts (Lubin et al., 2009). The ORELSE survey also utilizes the wide-field, multi-object spectroscopic capabilities of the Deep Multi-Object Imaging Spectrograph (DEIMOS; Faber et al. (2003)) on the Keck 10 m for much of its spectroscopic data.

By employing this wide range of sources, the ORELSE survey contains an unprecedented amount of spectroscopic coverage, as well as a sample size larger than most currently available. Through these efforts, the ORELSE survey contains  $\sim 11,000$  high quality spectroscopic objects, with 100 - 500 confirmed members per structure.

Hung et al. (2020) employed the rich data of the ORELSE survey in combination with the powerful Voronoi tessellation Monte-Carlo (VMC) mapping technique to search for serendipitous galaxy overdensities at  $0.55 < z < 1.37$  within 15 of the ORELSE fields to cover a combined spectroscopic footprint of 1.4 degrees. Hung et al. (2020) were able to discover and characterize 402 new overdensity candidates with precisely measured redshifts and unprecedented sensitivity in the 15 targeted ORELSE fields. With VMC mapping, they were able to measure precise redshifts, provide an estimate of the total gravitating mass, and maintain high levels of purity and completeness at  $z \sim 1$  with only moderate levels of spectroscopy.

For more comprehensive information on the ORELSE data and its expansion we refer the reader to Lubin et al. (2009) and Hung et al. (2020).

## 2.2. Star Formation Rates

### 2.2.1. UVIR SFR

Star-formation rates measured through IR and UV emission are drawn from work done in Tomczak et al. (2019). The SFR is estimated by adding contributions from obscured and unobscured young stellar populations as traced by IR and UV emission respectively. They used the calibration presented in Bell et al. (2005) scaled to the Chabrier (2003) IMF relation:

$$SFR_{UV+IR}[M_{\odot}/yr] = 1.09 \times 10^{-10} (2.2L_{UV} + L_{IR})[L_{\odot}] \quad (1)$$

Where  $L_{IR}$  is the bolometric infrared luminosity (8-1000  $\mu\text{m}$ ) derived by shifting the IR template (from Wuyts et al. (2008)) to the peak  $z$ , scaling the IR template to the observed 24  $\mu\text{m}$  flux, and integrating between 8-1000  $\mu\text{m}$  in the IR template's rest frame.  $L_{UV} = 1.5 \nu L_{\nu,2800}$  represents the rest-frame 121.6-300 nm luminosity estimated in Section 2.3 of Tomczak et al. (2019) with  $\nu$  being the frequency of light at 280 nm. In some cases, where there was low resolution in the far-IR imaging, fluxes were derived using TPHOT code (Merlin et al., 2015). TPHOT creates models of objects detected in a higher resolution image by convolving them to the resolution of the far-IR image. These models are simultaneously scaled to match the fluxes in the observed far-IR image which effectively accounts for the blending from neighboring objects. Additional information on the  $SFR_{UVIR}$  estimates can be found in Section 2.7 of Tomczak et al. (2019).

### 2.2.2. [OII] SFR

Another important star-formation metric used in this study comes from [O II]  $\lambda 3727$  Å line luminosity. This method has been calibrated against a variety of star formation indicators, and has been tested effectively (Moustakas et al., 2006; Weiner et al., 2007). The [O II] star formation rates used in this study are drawn from work done in Lemaux et al. (2010, 2014, 2017), as well as the extinction correction from Wuyts et al. (2013) and the FourStar Galaxy Evolution Survey (ZFOURGE) code described in Straatman et al. (2016). The catalogs used in this study contain [O II]-derived SFRs for all galaxies in ORELSE with a high-quality spectroscopic flag in the redshift range  $0.55 < z < 1.3$ . All of these galaxies have [O II] in the spectral range, have equivalent width measurements (EW)[O II]  $< -2.5$  Å (see Appendix A of Lemaux et al. (2010)), and are not NUVrJ quiescent by the criterion of Lemaux et al. (2014) to avoid emission not originating from star formation (Lemaux et al., 2010, 2017).

## 2.3. Estimating Environment

### 2.3.1. Local Environment

The local environmental densities used in this paper are estimated through a technique that employs a Voronoi Monte Carlo algorithm. For the ORELSE survey data, this procedure was developed and tested for performance in studies done by Lemaux et al. (2017), Tomczak

et al. (2017), and Hung et al. (2020). It has also already been used in a variety of studies over a broad redshift range  $0.6 < z < 4.6$  (e.g. Darvish et al. (2015); Shen et al. (2017, 2019); Rumbaugh et al. (2017); Cucciati et al. (2018); Pelliccia et al. (2019)). A Voronoi tessellation is the division of a 2D plane into a number of polygonal regions equal to the number of objects in that plane. The Voronoi cell of each object is defined as the region (or all the points that don't contain another object) closer to it than to any other object in the plane. Objects in high density regions therefore have small Voronoi cells, while objects in lower density regions have larger cells. The inverse area of the cell sizes can thus be used to measure the local density at the position of the object bounded by the cell.

In using VMC mapping, galaxies are partitioned into thin redshift slices with each slice spanning 3000 km/s in velocity space and overlapping by 1500 km/s from slice to slice. Each slice in redshift is then projected onto a 2-dimensional Voronoi tessellation that is calculated using the positions of the galaxies within it. Local environmental density is defined as the inverse of the area of a Voronoi cell multiplied by the square of the angular diameter distance at the corresponding mean redshift of the slice. The Voronoi maps are then projected onto a 2D grid of pixels sized 75 x 75 proper kpc. The local environmental overdensity at pixel (i,j) is defined as:

$$\log(1 + \delta_{gal}) \equiv \log\left(1 + \frac{\Sigma_{i,j} - \tilde{\Sigma}}{\tilde{\Sigma}}\right) \quad (2)$$

Where  $\Sigma_{i,j}$  is the density at pixel (i, j) and  $\tilde{\Sigma}$  is the median density of all the pixels where the map is reliable (i.e. where there is coverage in nearly all images and not near the edge of the detection image). The local overdensity for a given galaxy is set by the closest pixel in proximity in the transverse and redshift directions. As shown in Tomczak et al. (2017, 2019) and Lemaux et al. (2019) these local overdensities have been shown through tests to be strongly concordant with other density metrics and trace out the known structures extremely well.

### 2.3.2. Global Environment

In this study, the parameter  $\eta$  (defined by  $R_{proj}/R_{200} \times |\Delta v|/\sigma_v$ ) is used to determine global overdensity relative to an individual group or cluster and helps to separate different galaxy populations. Adopting definitions based on N-body simulations and other semi-analytic simulations (Noble et al., 2013),  $|\eta| < 0.1$  is the virialized core region,  $0.1 < |\eta| < 0.4$  is the intermediate region (possibly containing some backsplash galaxies, see Haines et al. (2012); Gill et al. (2005)), and  $0.4 < |\eta| < 2$  as the outer region containing galaxies that have recently been accreted, often known as the infall region (Haines et al., 2012). Galaxies with  $\eta > 2$  are located within the surrounding field and are not associated with any group or cluster. For further information see section 5.5.1.1 of Shen et al. (2017).



## 2.4. The Sample Selection

To select our sample, we filtered through the data from the 15 ORELSE fields that were expanded on by [Hung et al. \(2020\)](#). Since there is no one uniform method for gauging the SFR galaxies, we attempt to examine both  $SFR_{UVIR}$  and  $SFR_{[OII]}$  within the ORELSE survey to verify our findings. First, we identified field members that had contained the proper spectroscopic data (i.e. had measured  $SFR_{UVIR}$  and/or  $SFR_{[OII]}$ ) and filtered out any quiescent galaxies from that sample. We also made a cut in galaxy mass and only included galaxies with  $\log(M_*/M_\odot) \geq 9.4$ . Next, we made a cut in  $\log(\eta)$  with  $\log(\eta) \leq 0.3$  signaling the galaxies to be considered as cluster members, and  $\log(\eta) \geq 0.5$  identifying the galaxies in the nearby surrounding field for each cluster. Through these efforts we were left with 1,048 cluster galaxies for the  $SFR_{[OII]}$  sample and 897 galaxies for  $SFR_{UVIR}$  sample, as well as  $\sim 2,200$  and  $\sim 1,600$  field galaxies for the  $SFR_{[OII]}$  sample and  $SFR_{UVIR}$  sample respectively. It should be noted that the two samples for both cluster and field galaxies contain only star-forming galaxies (SFGs) and are overlapping samples rather than identical samples (some galaxies have both types of SFR measured, but other galaxies have only  $SFR_{[OII]}$  or  $SFR_{UVIR}$  recorded). Our sample is comparable in scope and size to the Gemini Observations of Galaxies in Rich Early Environments Survey (GOGREEN; [Balogh et al. \(2017\)](#); [Old et al. \(2020\)](#)).

To further narrow our sample, we bin the selected galaxies into 4 groups based on their corresponding cluster redshift and cluster mass. The 4 groups are as follows: low cluster redshift/low cluster mass, low cluster redshift/high cluster mass, high cluster redshift/low cluster mass, and high cluster redshift/high cluster mass (hereby referred to as LZLM, LZHM, HZLM, and HZHM) with the division for the high/low redshift and mass cuts being at  $z = 0.97$  and  $\log(M_*/M_\odot) = 13.9$  respectively. These 2 cuts were chosen to effectively distribute the ORELSE clusters from which the SFGs are drawn into comparable bins (see Table 1). Due to systematic issues in the data collection, a smaller number of galaxies are detected in the LZLM bin and, especially, the HZLM bin even though our bins all contain a similar number of clusters ([Hung et al., 2020](#)).

Bin	$N_{Clust}$	$N_{Gal} ([OII])$	$N_{Gal} (UVIR)$
$\log(M_*/M_\odot) < 13.9$	91	280	175
$\log(M_*/M_\odot) > 13.9$	92	768	722
$z < 0.97$	101	660	556
$z > 0.97$	82	388	341
LZLM	55	176	110
LZHM	46	484	446
HZLM	36	104	65
HZHM	46	284	276

Table 1: The distribution of clusters and cluster member galaxies within our cluster redshift and mass splits. Our chosen splits at  $z = 0.97$  and  $\log(M_*/M_\odot) = 13.9$  were chosen to create bins of approximately equal size for the clusters within our sample.

### 3. Results and Discussion

#### 3.1. Sample Comparison

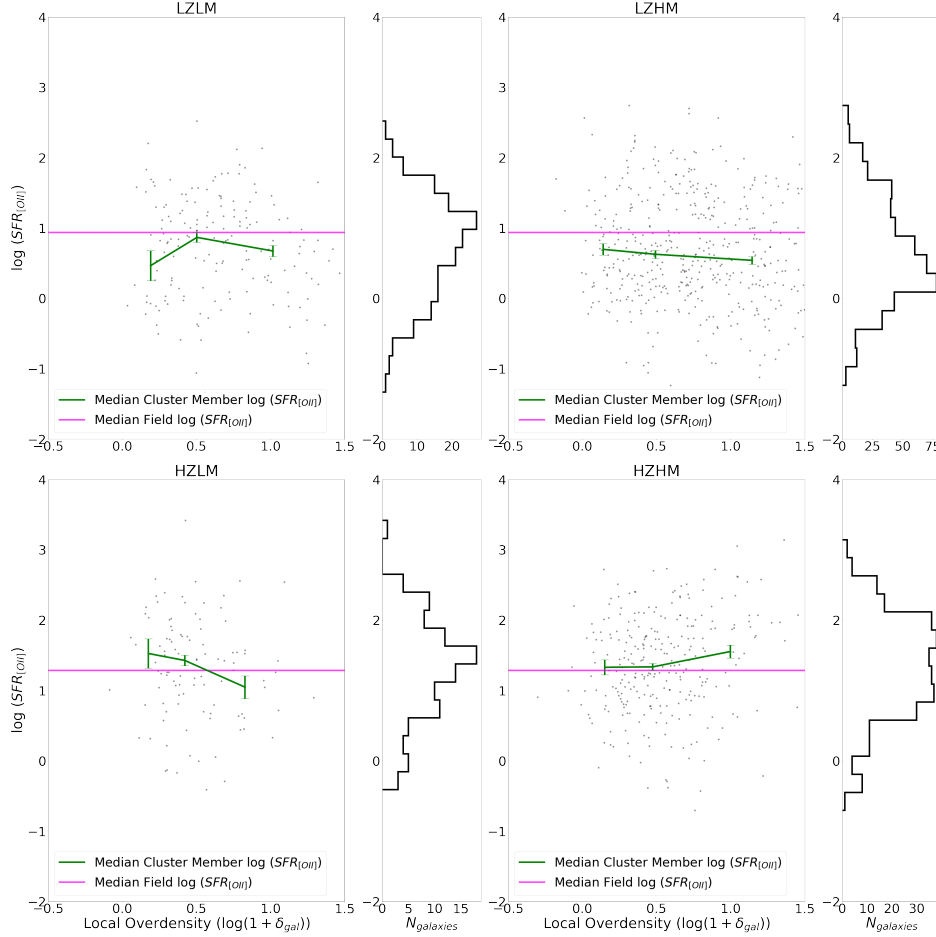


Figure 1: The relationship between  $SFR_{[OII]}$  and  $\log(1 + \delta_{gal})$  for cluster members and field members in 4 separate redshift/mass bins (see Section 2.4). Errors for Figure 1 and other subsequent similar figures (i.e. Figures 2, Figure 3, and Figure 4, etc.) were determined by taking the robust standard deviation (calculated through the median absolute deviation or MAD) divided by the  $\sqrt{N-1}$  with N being the number of galaxies located within that particular local/global overdensity bin.

Due to the limited nature of both of our SFR samples, we first compared the  $SFR_{UVIR}$  sample to the  $SFR_{[OII]}$  sample to probe for any inconsistencies. Using the 4 cluster redshift/mass bins described in Section 2.4, we examined the relationship between  $SFR_{[OII]}$  and  $\log(1 + \delta_{gal})$  to investigate discernible trends within that sample. In Figure 1, we plot  $SFR_{[OII]}$  against  $\log(1 + \delta_{gal})$  with the cluster medians, field medians, and individual galaxies all being displayed. The solid green lines with error bars and solid points represent the median  $SFR_{[OII]}$  for galaxies that are cluster members (i.e.  $\log(\eta) \leq 0.3$ ) within each bin. These median points were determined by taking median cluster galaxy  $SFR_{[OII]}$  and median cluster galaxy  $\log(1 + \delta_{gal})$  within 3  $\log(1 + \delta_{gal})$  bins that are as follows:  $\log(1 + \delta_{gal}) < 0.25$ ,



227  $0.25 < \log(1 + \delta_{gal}) < 0.75$ , and  $0.75 < \log(1 + \delta_{gal})$ . The solid magenta lines laid horizon-  
 228 tally across each plot represent the median field galaxy  $SFR_{[OII]}$  from our sample within  
 229 that redshift (lower redshift for the LZLM and LZHM panels, and higher redshift for the  
 230 HZLM and HZHM panels). The gray points are included for reference and are the individual  
 231 galaxies that contribute to the solid median cluster member  $SFR_{[OII]}$  line. On the right of  
 232 each panel lies a histogram showing the distribution of cluster members by  $SFR_{[OII]}$ .

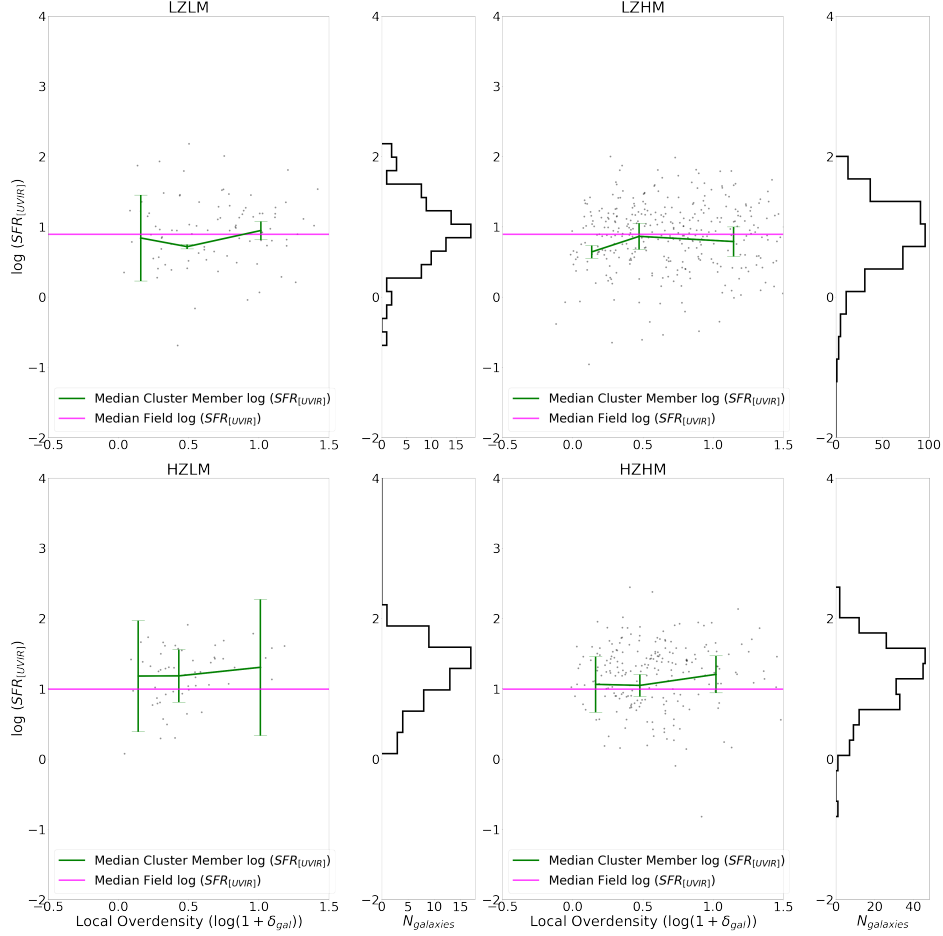


Figure 2: The relationship between  $SFR_{UVIR}$  and  $\log(1 + \delta_{gal})$  for cluster members and field members in the 4 separate redshift/mass bins of Section 2.4. Similar to Figure 1, the solid green lines represent cluster member median  $SFR_{UVIR}$  and the solid magenta lines represent the median field  $SFR_{UVIR}$ . For reference, the individual galaxies and a histogram of the  $SFR_{UVIR}$  distribution are plotted for cluster galaxies in the  $SFR_{UVIR}$  sample that had physical  $SFR_{UVIR}$  values.

233 The 4 panel structure of Figure 1 allows for close comparison between varying cluster mass  
 234 and between our higher and lower redshift bins. In the upper panels (lower redshifts), the  
 235 median SFRs across the entire  $\log(1 + \delta_{gal})$  scale are consistently suppressed (see Table 2)  
 236 when compared to the corresponding field galaxies at similar redshift. This behavior is  
 237 expected, for the various environment processes of clusters in low redshifts often quenches  
 238 SFR (Lewis et al., 2002; Gómez et al., 2003; Cooper et al., 2008). However, in the higher

redshift (lower) panels of Figure 1, this behavior is no longer observed. The median  $SFR_{[OII]}$  for the cluster galaxies at high redshift fail to display the same suppression as those at lower redshift with the median  $SFR_{[OII]}$  being similar—or even enhanced—when compared to field galaxies at the same redshift (see Table 2).

Bin and Point	Diff From Field	Bin and Point	Diff From Field
LZLM Left	-0.594 $\sigma$	HZLM Left	0.328 $\sigma$
LZLM Mid	-0.089 $\sigma$	HZLM Mid	0.194 $\sigma$
LZLM Right	-0.332 $\sigma$	HZLM Right	-0.321 $\sigma$
LZHM Left	-0.302 $\sigma$	HZHM Left	0.062 $\sigma$
LZHM Mid	-0.391 $\sigma$	HZHM Mid	0.070 $\sigma$
LZHM Right	-0.499 $\sigma$	HZHM Right	0.366 $\sigma$

Table 2: The difference in  $\sigma$  between the median cluster  $SFR_{[OII]}$  points and the median field galaxy lines in the log scale. All of the cluster medians in our lower redshift bins are reduced compared to the field, whereas most of the cluster medians in our higher redshift bins are comparable or enhanced when compared to the field galaxies.

In Figure 2, we plot  $SFR_{UVIR}$  against  $\log(1 + \delta_{gal})$  to see if trend observed in the  $SFR_{[OII]}$  sample holds with another measure of SFR. Plotted in a similar manner as Figure 1, Figure 2 displays the cluster medians, field medians, and individual galaxies for each of the 4 cluster redshift/mass bins. However, due to negative IR flux values from the MIPS measurements, and thus nonphysical  $SFR_{UVIR}$  values included within the ORELSE catalogs, the full distribution of our catalog sample (all  $\sim 1,200$  galaxies) includes some galaxies with these dubious measurements. Only the individual galaxies with physical  $SFR_{UVIR}$  values are plotted in Figure 2, but our full sample distribution was used to determine the median cluster member  $SFR_{[UVIR]}$  and  $\log(1 + \delta_{gal})$  points, as well as the field median  $SFR_{UVIR}$  lines, in a similar manner to Tomczak et al. (2019). Many of the negative IR flux values were the result of noise, and the overall signal is only reliable by using the full distribution rather than single point statistics. This correction was not needed for the  $SFR_{[OII]}$  data for these imperfections do not exist within that sample.

Figure 2 and the  $SFR_{UVIR}$  sample fails to display the same trend that was previously observed in Figure 1 with the  $SFR_{[OII]}$  sample. In all 4 cluster redshift/mass bins, cluster member  $SFR_{UVIR}$  is comparable to field  $SFR_{UVIR}$  at all local overdensities and very little suppression is seen in any bin, whereas this lack of suppression is only seen in the HZLM and HZLM bins for the  $SFR_{[OII]}$  sample. This difference in observation can be attributed to the lack of detection at the lower end of our  $SFR_{UVIR}$  sample (around  $\log(SFR_{UVIR}) < 0.5$ ). There is a significant lack of low IR flux coverage in the MIPS measurements which in turn results in few galaxies with low  $SFR_{UVIR}$  being detected.

In Figure 3, we plot  $SFR_{[OII]}$  against  $\log(1 + \delta_{gal})$  again with median cluster member  $SFR_{[OII]}$ , median field  $SFR_{[OII]}$ , and individual galaxies all being shown, but only for both cluster and field galaxies with  $\log(SFR_{[OII]}) \geq 0.5$ . The resulting Figure 3 bears a striking similarity to Figure 2 in the LZHM and HZHM bins on the right where most of our two

268 samples are concentrated. The median cluster SFR location relative to the median field  
 269 SFR, the shape of the median cluster SFR curves, and in the distribution of SFR within the  
 270 histograms in both those bins between Figure 2 and Figure 3 are in agreement.

271 Both Figure 2 and Figure 3 show the same lack of differential evolution between median clus-  
 272 ter SFR and median field SFR. Therefore, we conclude that the two different SFR samples  
 273 are comparable, but there exists more depth within the  $SFR_{[OII]}$  sample (i.e more low SFR  
 274 galaxies being detected) that is simply absent from the  $SFR_{UVIR}$  sample. The observed  
 275 trend within the  $SFR_{[OII]}$  sample could never be seen within the  $SFR_{UVIR}$  sample due to  
 276 the lack of low IR flux coverage resulting from limitations within the MIPS spectroscopy.  
 277 If the  $SFR_{UVIR}$  sample had increased depth, we could possibly observe the same trend as  
 278 the  $SFR_{[OII]}$  sample, but we cannot be certain. Thus, we can only proceed with further  
 279 investigation of the  $SFR_{[OII]}$  sample.

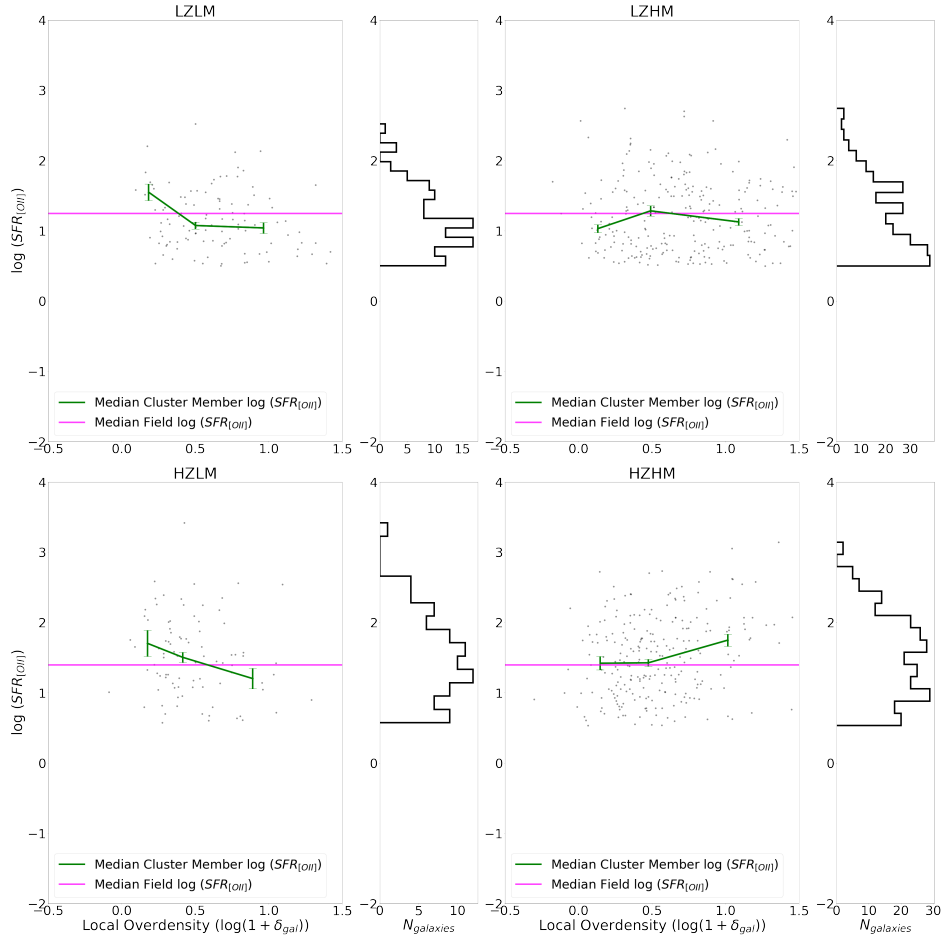


Figure 3: The relationship between  $SFR_{[OII]}$  and  $\log(1 + \delta_{gal})$  for cluster members and field members in the 4 separate redshift/cluster mass bins is displayed in a similar style as the previous 2 figures. Only galaxies with  $\log(SFR_{[OII]}) \geq 0.5$  are included to display the detection bias within the  $SFR_{UVIR}$  sample.

### 3.2. $SFR_{[OII]}$ Sample Findings

We plot Figure 4 in the same manner as previous figures, but the galaxies have now been further binned according to their mass based on the cuts of Tomczak et al. (2019) (i.e.  $9.4 < \log(M_*/M_\odot) < 10.1$ ,  $10.1 < \log(M_*/M_\odot) < 10.8$ , and  $10.8 < \log(M_*/M_\odot)$ ). As previously shown in Figure 1, median cluster  $SFR_{[OII]}$  is suppressed relative to galaxies in the field for the LZLM and LZHM bins, and this observation holds in Figure 4 when our  $SFR_{[OII]}$  sample is split according to galaxy mass (see Table 3). In Figure 4, we also find that in the HZLM and HZHM bins all cluster member galaxies are star forming at rates comparable to galaxies in the field, and it is primarily the intermediate mass galaxies in the HZHM bin that are enhanced relative to intermediate mass field galaxies (on average by  $\sim 0.5\sigma$ ). Additionally, high and intermediate mass galaxies in the HZLM and HZHM bins are star forming more than the corresponding galaxies in the LZLM and LZHM bins at almost double the rate in the log scale, and the distribution of galaxies for high and intermediate galaxies by  $SFR_{[OII]}$  is shifted upwards in our higher redshift bins. This suggests that the epoch of massive quenching within clusters has yet to be reached in our higher redshift sample and is evident through our redshift split at  $z = 0.97$ .

Bin	$M_{gal}$ & Point	Diff From Field	Bin	$M_{gal}$ & Point	Diff From Field
LZLM	Low Left	0.582 $\sigma$	HZLM	Low Left	-0.077 $\sigma$
LZLM	Low Mid	0.187 $\sigma$	HZLM	Low Mid	0.149 $\sigma$
LZLM	Low Right	-0.125 $\sigma$	HZLM	Low Right	-0.168 $\sigma$
LZLM	Mid Left	-1.270 $\sigma$	HZLM	Mid Left	0.168 $\sigma$
LZLM	Mid Mid	-0.384 $\sigma$	HZLM	Mid Mid	0.088 $\sigma$
LZLM	Mid Right	-0.624 $\sigma$	HZLM	Mid Right	0.106 $\sigma$
LZLM	High Left	0.367 $\sigma$	HZLM	High Left	0.609 $\sigma$
LZLM	High Mid	-0.043 $\sigma$	HZLM	High Mid	-0.184 $\sigma$
LZLM	High Right	-0.572 $\sigma$	HZLM	High Right	N/A
LZHM	Low Left	-0.029 $\sigma$	HZHM	Low Left	-0.141 $\sigma$
LZHM	Low Mid	-0.644 $\sigma$	HZHM	Low Mid	0.172 $\sigma$
LZHM	Low Right	-0.476 $\sigma$	HZHM	Low Right	-0.255 $\sigma$
LZHM	Mid Left	-0.695 $\sigma$	HZHM	Mid Left	0.537 $\sigma$
LZHM	Mid Mid	-0.674 $\sigma$	HZHM	Mid Mid	0.208 $\sigma$
LZHM	Mid Right	-0.719 $\sigma$	HZHM	Mid Right	0.622 $\sigma$
LZHM	High Left	-0.752 $\sigma$	HZHM	High Left	0.032 $\sigma$
LZHM	High Mid	-0.196 $\sigma$	HZHM	High Mid	0.074 $\sigma$
LZHM	High Right	-0.364 $\sigma$	HZHM	High Right	0.030 $\sigma$

Table 3: The difference in  $\sigma$  between the cluster member median  $SFR_{[OII]}$  points and the field galaxy median  $SFR_{[OII]}$  lines split by galaxy mass. Intermediate mass galaxies in our HZHM bin experience the most enhancement relative to the field.

However, it is natural for galaxies of higher mass to have higher SFRs for they have more star forming material to convert into stars. Therefore, it is crucial to also examine the

298 efficiency of star formation through the metric of specific star-formation rate ( $sSFR$ ; defined  
 299 as the  $SFR$  of the galaxy divided by its stellar mass) which removes the bias towards more  
 300 massive galaxies. Figure 5 takes the same galaxies of the  $SFR_{[OII]}$  sample, but instead  
 301 displays the relationship between  $sSFR_{[OII]}$  and  $\log(1 + \delta_{gal})$ . As expected, suppression,  
 302 especially in galaxies that are members of high mass clusters, can be seen in the lower  
 303 redshift bins (LZLM and LZHM) for galaxies of all masses, and, on average, the  $sSFR_{[OII]}$   
 304 for galaxies contained within clusters is lower when compared to those within the nearby  
 305 field (see Table 4). A lack of suppression, and in some cases enhancement, of  $sSFR_{[OII]}$   
 306 is seen for galaxies in the higher redshift HZLM and HZHM bins when compared to the  
 307 similar mass field galaxies. The higher redshift galaxies continue to exhibit more  $sSFR_{[OII]}$   
 308 than what is traditionally seen at lower redshift signaling that at  $z > 0.97$  the environment  
 309 processes seen in the more local universe have yet to take effect.

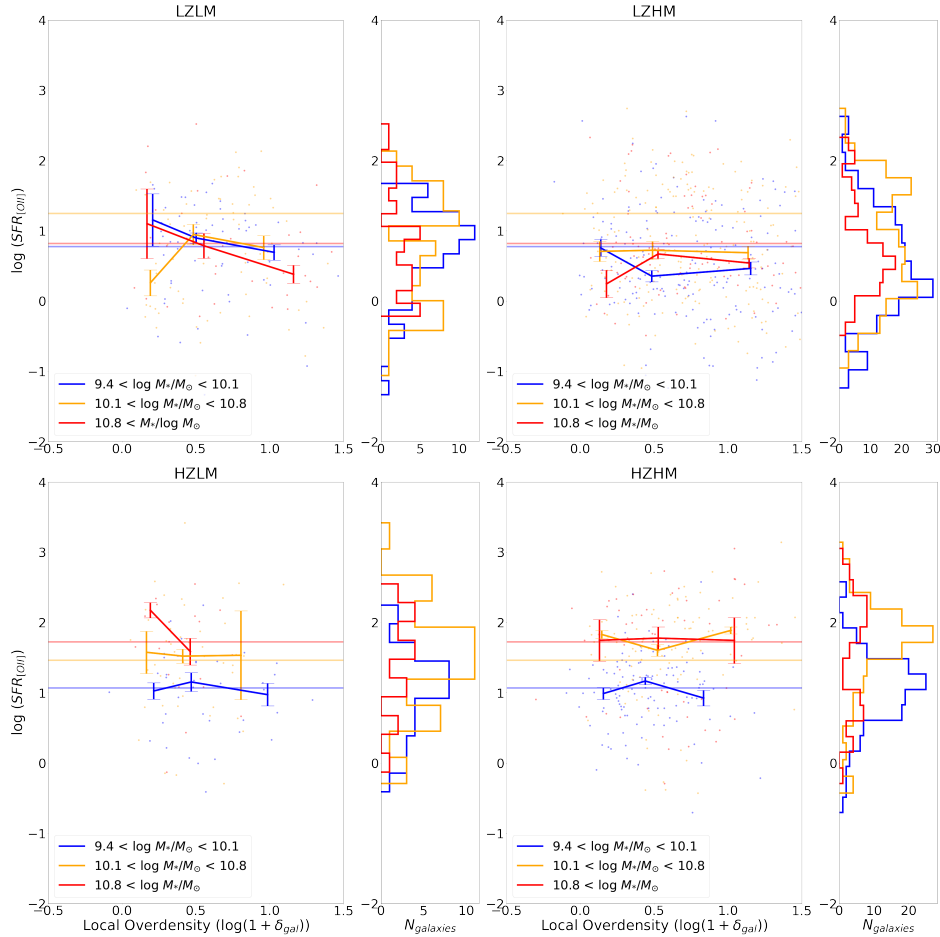


Figure 4: The relationship between  $SFR_{[OII]}$  and  $\log(1 + \delta_{gal})$  for cluster members and field members in the 4 redshift/cluster mass bins. Both the field and cluster galaxies are further binned by their stellar mass to highlight specific changes. This further binning is reflected in the cluster member medians, the field medians, the individual galaxy scatter, and histograms with the lowest mass galaxies being represented in blue, the intermediate mass galaxies being represented in orange, and the highest mass galaxies in red.

Bin	$M_{gal}$ & Point	Diff From Field	Bin	$M_{gal}$ & Point	Diff From Field
LZLM	Low Left	0.633 $\sigma$	HZLM	Low Left	-0.262 $\sigma$
LZLM	Low Mid	0.059 $\sigma$	HZLM	Low Mid	0.109 $\sigma$
LZLM	Low Right	-0.301 $\sigma$	HZLM	Low Right	-0.181 $\sigma$
LZLM	Mid Left	-1.397 $\sigma$	HZLM	Mid Left	0.140 $\sigma$
LZLM	Mid Mid	-0.422 $\sigma$	HZLM	Mid Mid	0.034 $\sigma$
LZLM	Mid Right	-0.521 $\sigma$	HZLM	Mid Right	-0.136 $\sigma$
LZLM	High Left	-0.029 $\sigma$	HZLM	High Left	0.519 $\sigma$
LZLM	High Mid	-0.066 $\sigma$	HZLM	High Mid	-0.232 $\sigma$
LZLM	High Right	-0.703 $\sigma$	HZLM	High Right	N/A
LZHM	Low Left	-0.078 $\sigma$	HZHM	Low Left	-0.174 $\sigma$
LZHM	Low Mid	-0.645 $\sigma$	HZHM	Low Mid	0.111 $\sigma$
LZHM	Low Right	-0.544 $\sigma$	HZHM	Low Right	-0.298 $\sigma$
LZHM	Mid Left	-0.713 $\sigma$	HZHM	Mid Left	0.584 $\sigma$
LZHM	Mid Mid	-0.753 $\sigma$	HZHM	Mid Mid	0.202 $\sigma$
LZHM	Mid Right	-0.933 $\sigma$	HZHM	Mid Right	0.628 $\sigma$
LZHM	High Left	-0.971 $\sigma$	HZHM	High Left	0.105 $\sigma$
LZHM	High Mid	-0.203 $\sigma$	HZHM	High Mid	0.076 $\sigma$
LZHM	High Right	-0.351 $\sigma$	HZHM	High Right	0.050 $\sigma$

Table 4: The difference in  $\sigma$  between the cluster member median  $sSFR_{[OII]}$  points and the field galaxy median  $SFR_{[OII]}$  lines split by galaxy mass. Changing our metric from SFR to sSFR does not affect the observed trend within the  $SFR_{[OII]}$  sample.

Figure 6 further expands on this underlying trend within our  $SFR_{[OII]}$  sample by plotting  $SFR_{[OII]}$  in relation to global overdensity within the cluster ( $\log(\eta)$ ). Median  $SFR_{[OII]}$  for cluster members are instead binned by  $\log(\eta)$  at cuts of  $\log(\eta) < -1$ ,  $-1 < \log(\eta) < -0.4$ , and  $-0.4 < \log(\eta) < 0.3$  (corresponding to the  $\eta$  definitions seen in Section 2.3.2). By changing over from local to global overdensity, the same trend in  $SFR_{[OII]}$  still holds regardless of overdensity measurement. Suppression for high and intermediate mass galaxies in clusters occurs almost exclusively in our lower redshift bins, while our higher redshift bins seem to be immune to similar suppression. The only notable exception is in the core of clusters ( $\log(\eta) < -1$ ) in the HZHM bin where suppression is seen for galaxies with the highest stellar mass.

Figure 7 gives a detailed look into the relation of  $sSFR_{[OII]}$  and  $\log(\eta)$ . Akin to previous figures, suppression seems to be a feature of star forming galaxies in our low redshift clusters almost exclusively. Intermediate and high mass galaxies in our higher redshift bins are immune to this same suppression and are star forming with more efficiency than their low redshift bin counterparts with the only exception being high mass galaxies in the cores of clusters. In the HZHM bin, we observe the repeated enhancement in star-formation by the intermediate mass galaxies compared to similar galaxies in the field.

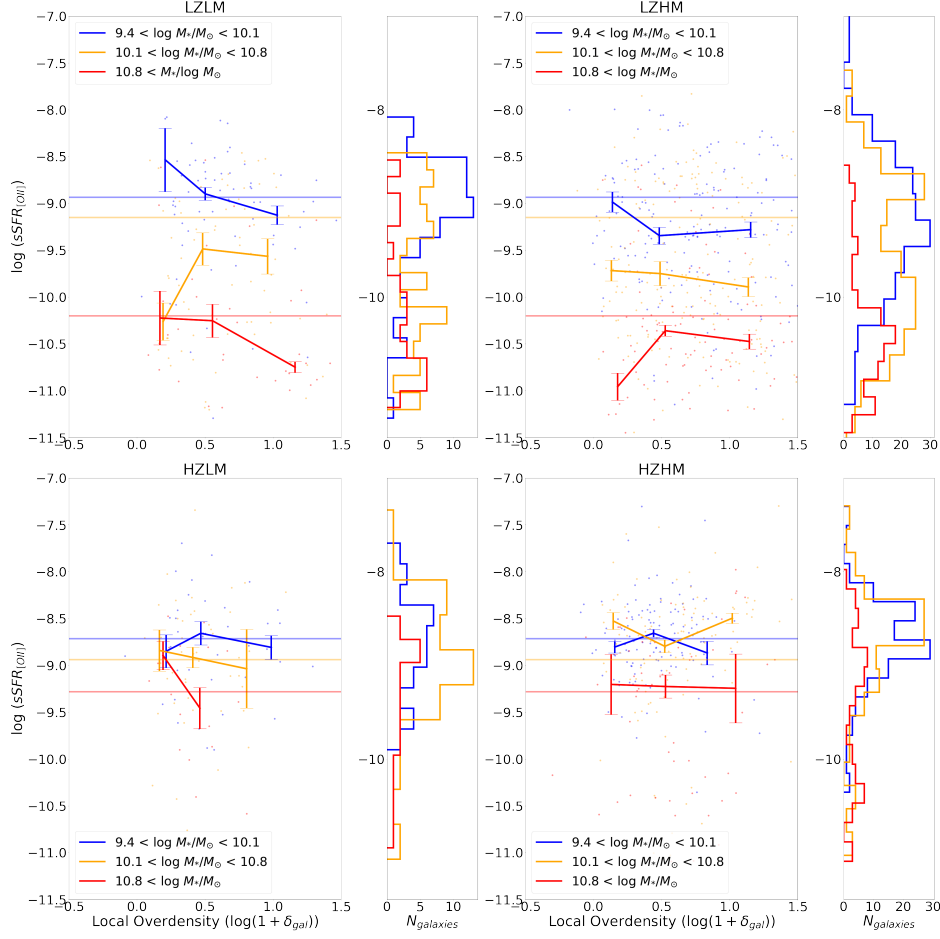


Figure 5: The relationship between  $sSFR_{[OII]}$  and  $\log(1+\delta_{gal})$  for cluster members and field members in our 4 separate redshift/mass bins. Field galaxy median  $sSFR_{[OII]}$ , cluster member median  $sSFR_{[OII]}$ , and individual galaxies are all over-plotted with a histogram  $sSFR_{[OII]}$  to the right of each quadrant for reference. Suppression can be seen in all cluster members at lower redshifts, while at higher redshifts — and especially for galaxies with intermediate mass in the HZHM bin — this suppression is removed.

We compared the distribution of  $\log(sSFR_{[OII]})$  between cluster member galaxies in the three galaxy mass bins across our 4 cluster redshift/mass bins, as well as against the corresponding field galaxies within each bin using two-sample KS tests. Two-sample KS tests allow us to determine how likely or unlikely two samples are to be drawn from the same parent population by comparing the determined KS statistic to the samples critical value (i.e. when the KS statistic is higher than the critical value, the two distributions are different). We performed KS tests at a 95% confidence level ( $\alpha = 0.05$ ). Through these tests, we determined that the the overall populations between the 4 cluster redshift/mass bins were similar when compared by similar redshift (ex. between LZLM and LZHM; see Table 5), but drastically different when compared by similar cluster mass.

Our two-sample KS tests for cluster member galaxies versus field galaxies supports our findings within the  $SFR_{[OII]}$  sample. We find that in our lower redshift bins the two populations



Cluster Bins Compared	KS Statistic	Critical Value
LZLM and HZLM	0.269	0.157
LZHM and HZHM	0.424	0.094
LZLM and LZHM	0.110	0.111
HZLM and HZHM	0.104	0.146

Table 5: Two-sample KS statistic results for all cluster member galaxies across our 4 cluster redshift/mass bins. The tests were performed with  $\alpha = 0.05$ .

(cluster member and field) likely come from different distributions, thus reinforcing the suppressed nature of the cluster member galaxies (see Table 6). However, in our higher redshift bins, the two populations come from the same distribution which corroborates the fact that the cluster member galaxies have similar SFRs to the field galaxies. In our higher redshift bin, the standard and expected cluster quenching has not yet rid the cluster member galaxies of their star-forming material.

Cluster Bin	KS Statistic	Critical Value
LZLM	0.135	0.010
LZHM	0.198	0.065
HZLM	0.063	0.132
HZHM	0.075	0.086

Table 6: Two-sample KS test results for the comparison of cluster member galaxies to field galaxies. Tests were performed at a 95% confidence level.

### 3.3. "4H" Galaxies

Contributing to the high SFRs and sSFRs seen in the HZHM bin throughout this paper has been a curious population of galaxies not seen in our other 3 cluster redshift/mass bins. These galaxies are high in stellar mass and exist within the highest density environments at high redshift, but are still star-forming at a high rate. We dub them "4H" galaxies for their 4 different "high" attributes. Table 7 lists 14 "4H" candidates and some of their properties. To be considered as "4H", we selected only the galaxies that existed at environments of  $\log(1 + \delta_{gal}) \geq 1$ , were star-forming at an efficiency of  $sSFR_{[OII]} \geq -8.5 M_{*/\odot}$  and had a mass of  $\log(M_*/M_\odot) \geq 10.1$ .

Figure 8 shows the location of the 14 galaxies we have tagged as "4H" candidates. This figure is essentially the HZHM panel of Figure 5 pulled out to show additional detail. Only the individual galaxies have been plotted with the median cluster member  $sSFR_{[OII]}$  and median field  $sSFR_{[OII]}$  being removed. In Figure 8, the "4H" galaxy candidates all lie in the upper right of the figure in the region of highest overdensity, as well as highest star-formation efficiency. These galaxies are unusual due to their high mass and high  $sSFR_{[OII]}$  for them to exist at high overdensity in the redshift slice of the ORELSE survey. Subsequent work

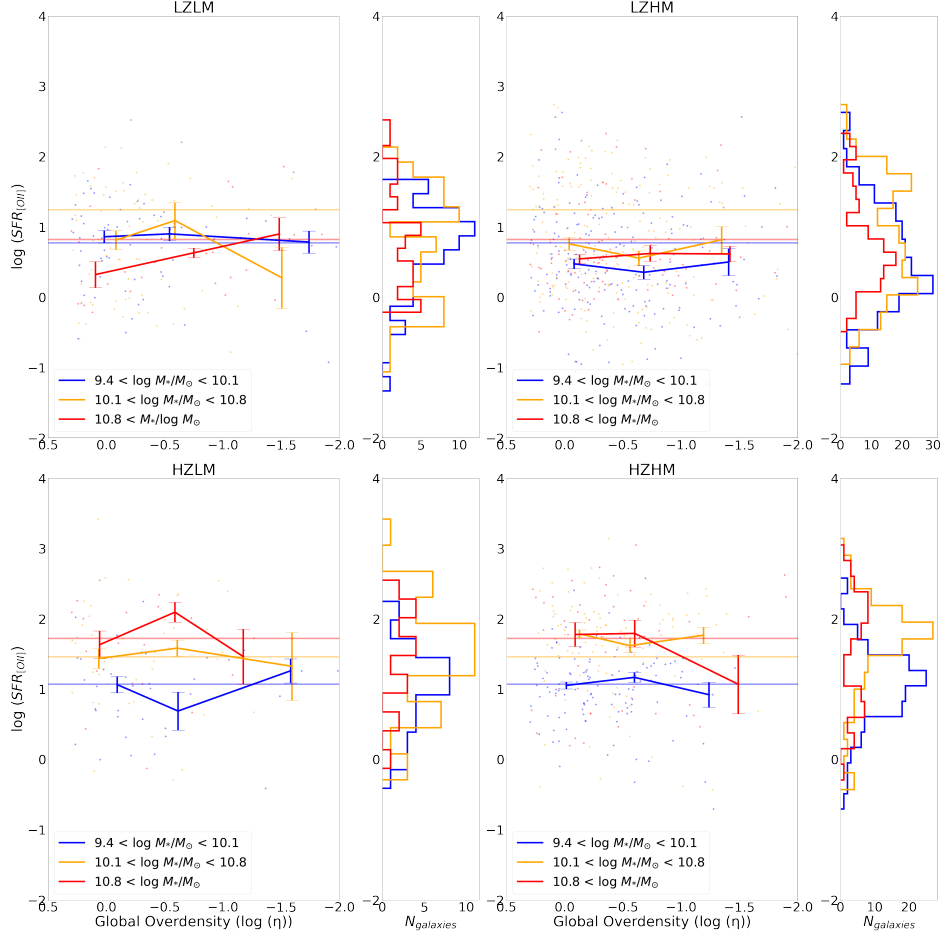


Figure 6: The relationship between  $SFR_{[OII]}$  and  $\log(\eta)$  for cluster members and field members in our 4 separate redshift/cluster mass bins. Changing the measure of overdensity does little to alter the overall trends within our  $SFR_{[OII]}$  sample.

will investigate these galaxies in an effort to shed more light on their properties and their origin.

#### 4. Conclusions

In this paper, we examine the relationship between SFR and environmental overdensity in two separate samples of 1,048 and 897 galaxies using data drawn from the ORELSE survey around  $z \sim 1$ . Two different indicators of SFR,  $[O II] \lambda 3727 \text{ \AA}$  and UV+IR emission, are looked at in relation to two different overdensity indicators,  $\log(1 + \delta_{gal})$  (local overdensity) and  $\log(\eta)$  (distance from the cluster center). Our two samples are split by cluster redshift and mass into 4 roughly equal bins of galaxy clusters to investigate impact of environment on star formation.

One of our samples drew from galaxies with measured  $SFR_{[OII]}$  and the other from galaxies

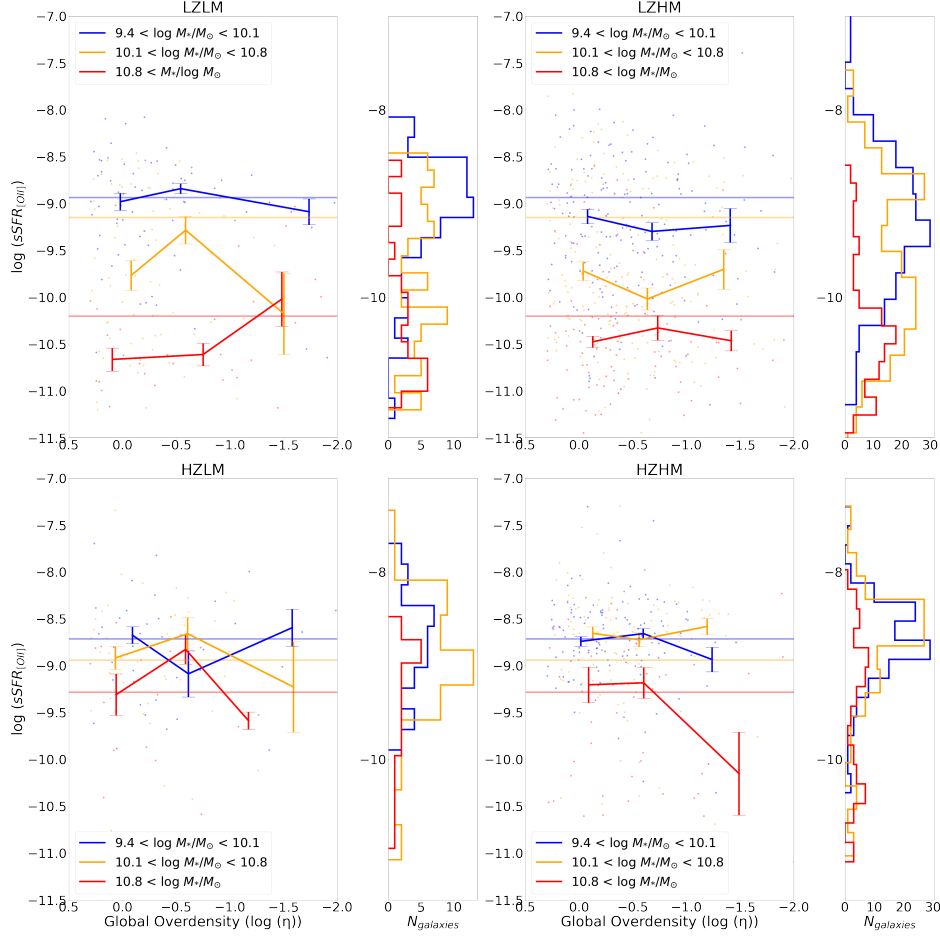


Figure 7: The relationship between  $sSFR_{[OII]}$  and  $\log(\eta)$  for cluster members and field members in 4 separate redshift/cluster mass bins. In the higher redshift bins (HZLM and HZHM), only the highest mass stars existing at the cores of clusters experience significant suppression.

with measured  $SFR_{UVIR}$ . These two samples are overlapping, but were providing conflicting results regarding star-formation and environment. We cut the  $SFR_{[OII]}$  sample at  $\log(SFR_{[OII]}) \geq 0.5$  and found that only then the two samples agreed. This lead us to the realization that the  $SFR_{UVIR}$  lacked significant low IR flux coverage, and thus was missing most of the galaxies in the ORELSE fields with  $\log(SFR_{UVIR}) < 0.5$ . The  $SFR_{[OII]}$  sample and  $SFR_{UVIR}$  are comparable, but not on an individual galaxies basis. Overall population statistics must be utilized to make any sense of the two SFR metrics relative to one another. We proceeded to further break down only the  $SFR_{[OII]}$  sample since the  $SFR_{UVIR}$  could only be trusted for its larger medians and not for its individual statistics. Our study revealed what should be a cautionary tale for those using UV+IR emission to study SFR in galaxies at  $z = 1$  and beyond. Data from MIPS and other similar data sets should be examined more closely to reveal their biases towards galaxies with larger IR flux.

In the  $SFR_{[OII]}$  sample, we find that galaxies in our higher redshift bins and in more

Field	Structure	$\log(sSFR_{[OII]})$	$\log(1 + \delta_{gal})$	$\log(M_*/M_\odot)$
CL1137	743	-7.97804	1.04275	11.03
CL1137	743	-8.20592	1.0482	10.82
CL1429	A	-7.29731	1.35974	10.44
RXJ1053	Hz	-7.95245	1.20364	10.53
SC0849	C	-8.22810	1.0436	10.85
SC0849	C	-8.27406	1.11148	10.82
SC0849	A	-8.29696	1.45393	10.37
RXJ0910	308	-8.31075	1.18216	10.38
SC1324	Hz	-8.38202	1.0216	10.27
SC1604	1398	-8.40238	1.16944	10.18
SC1604	1398	-8.48441	1.16145	10.24
XLSS005	2848	-8.32921	1.12376	10.31
XLSS005	2848	-8.27778	1.13236	10.18
XLSS005	A	-8.39883	1.03145	10.75

Table 7: "4H" galaxy candidates and their various properties. There exists no discernible trend as to which field or cluster these galaxies originate from.

dense environments exhibit higher SFRs and higher SFR efficiency relative to field galaxies. The SFR and sSFR of the higher redshift galaxies are also much higher than similar mass galaxies in our lower redshift bins. We further break down our  $SFR_{[OII]}$  sample by galaxy mass and find that this trend is especially true for the more massive galaxies (i.e. those in the intermediate and high stellar mass bins). We conclude that  $z \sim 1$  is the epoch for massive SFR change within galaxy clusters for slightly at higher redshift the galaxies display significant SF that is already absent by  $z < 1$ . Though selection bias within our sample has yet to be fully explored, we are confident that our results will hold. Both the field galaxies and cluster member galaxies come from the same DEIMOS spectroscopy, so the comparisons between them help to confirm our current results validity. Galaxies residing in clusters in our sample undergo massive amounts of quenching around  $z \sim 1$ , but the physical mechanisms behind this quenching remain unclear and continued work on this project will aim to shed light on this issue. A comparison to large-scale simulations has not yet been preformed, but future work with this project will also pursue that in an attempt to confirm our findings, specifically this observation with high- and intermediate-mass galaxies.

We also observed a population of high-mass galaxies in the highest density environments in our highest redshift bin that posses high star formation rates which have not been previously seen. These so called "4H" galaxies seem to be a unique feature of clusters at  $z > 1$  and could be one of the driving components behind the enhanced SFR we observed in our higher redshift bins. Further studies will be conducted to pursue these galaxies and their properties.

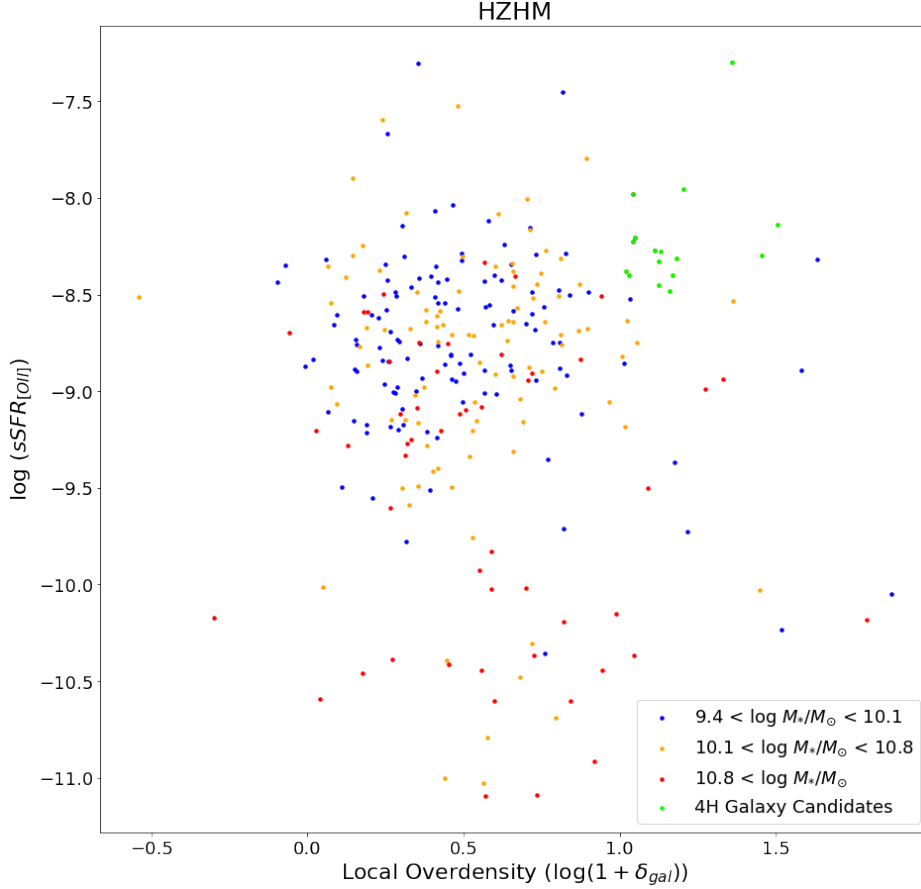


Figure 8: The HZHM panel of Figure 5 pulled out to show additional detail. Only the individual galaxies have been plotted with the median cluster member  $sSFR_{[OII]}$  and median field  $sSFR_{[OII]}$  being removed. The cluster members are binned by cluster mass with blue representing the lowest mass galaxies, yellow representing the intermediate mass galaxies, and red representing the highest mass galaxies. Galaxies that we have coined the term "4H" for are plotted in lime green ("4H" standing for high redshift, high cluster mass, high  $SFR_{[OII]}$ , and high local overdensity).

## Acknowledgements

Finn Giddings acknowledges support from Research Experience for Undergraduate program at the Institute for Astronomy, University of Hawaii-Manoa funded through NSF grant #2050710. Finn Giddings would like to thank the Institute for Astronomy for their hospitality during the course of this project. This work is based on observations made by Subaru, UKIRT, and Keck. We wish to extend our special thanks to those of Hawaiian ancestry on whose sacred mountain of Maunakea we are privileged to be guests. The observations presented herein would not have been possible without their generosity.

## References

- M. L. Balogh, S. L. McGee, A. Mok, A. Muzzin, R. F. J. van der Burg, R. G. Bower, A. Finoguenov, H. Hoekstra, C. Lidman, J. S. Mulchaey, A. Noble, L. C. Parker, M. Tanaka, D. J. Wilman, T. Webb, G. Wilson, and H. K. C. Yee. Evidence for a change in the dominant satellite galaxy quenching mechanism at  $z = 1$ . *MNRAS*, 456(4):4364–4376, Mar. 2016. doi: 10.1093/mnras/stv2949.
- M. L. Balogh, D. G. Gilbank, A. Muzzin, G. Rudnick, M. C. Cooper, C. Lidman, A. Biviano, R. Demarco, S. L. McGee, J. B. Nantais, A. Noble, L. Old, G. Wilson, H. K. C. Yee, C. Bellhouse, P. Cerulo, J. Chan, I. Pintos-Castro, R. Simpson, R. F. J. van der Burg, D. Zaritsky, F. Ziparo, M. V. Alonso, R. G. Bower, G. De Lucia, A. Finoguenov, D. G. Lambas, H. Muriel, L. C. Parker, A. Rettura, C. Valotto, and A. Wetzel. Gemini Observations of Galaxies in Rich Early Environments (GOGREEN) I: survey description. *MNRAS*, 470(4):4168–4185, Oct. 2017. doi: 10.1093/mnras/stx1370.
- E. F. Bell, C. Papovich, C. Wolf, E. Le Floch, J. A. R. Caldwell, M. Barden, E. Egami, D. H. McIntosh, K. Meisenheimer, P. G. Pérez-González, G. H. Rieke, M. J. Rieke, J. R. Rigby, and H.-W. Rix. Toward an Understanding of the Rapid Decline of the Cosmic Star Formation Rate. *ApJ*, 625(1):23–36, May 2005. doi: 10.1086/429552.
- E. L. Blanton, M. D. Gregg, D. J. Helfand, R. H. Becker, and R. L. White. Discovery of a High-Redshift ( $z=0.96$ ) Cluster of Galaxies Using a FIRST Survey Wide-Angle-Tailed Radio Source. *AJ*, 125(4):1635–1641, Apr. 2003. doi: 10.1086/368140.
- A. Boselli, S. Boissier, L. Cortese, and G. Gavazzi. The effect of ram-pressure stripping and starvation on the star formation properties of cluster galaxies. *Astronomische Nachrichten*, 330:904, Dec. 2009. doi: 10.1002/asna.200911259.
- O. Boulade, X. Charlot, P. Abbon, S. Aune, P. Borgeaud, P.-H. Carton, M. Carty, J. Da Costa, H. Deschamps, D. Desforge, D. Eppellé, P. Gallais, L. Gosset, R. Granelli, M. Gros, J. de Kat, D. Loiseau, J. . Ritou, J. Y. Roussé, P. Starzynski, N. Vignal, and L. G. Vigroux. MegaCam: the new Canada-France-Hawaii Telescope wide-field imaging camera. In M. Iye and A. F. M. Moorwood, editors, *Instrument Design and Performance for Optical/Infrared Ground-based Telescopes*, volume 4841 of *Society of Photo-Optical Instrumentation Engineers (SPIE) Conference Series*, pages 72–81, Mar. 2003. doi: 10.1117/12.459890.
- G. Chabrier. Galactic Stellar and Substellar Initial Mass Function. *PASP*, 115(809):763–795, July 2003. doi: 10.1086/376392.
- D. Christlein and A. I. Zabludoff. Disentangling Morphology, Star Formation, Stellar Mass, and Environment in Galaxy Evolution. *ApJ*, 621(1):201–214, Mar. 2005. doi: 10.1086/427427.
- J. M. Colberg, S. D. M. White, N. Yoshida, T. J. MacFarland, A. Jenkins, C. S. Frenk, F. R. Pearce, A. E. Evrard, H. M. P. Couchman, G. Efstathiou, J. A. Peacock, P. A. Thomas, and Virgo Consortium. Clustering of galaxy clusters in cold dark matter universes. *MNRAS*, 319(1):209–214, Nov. 2000. doi: 10.1046/j.1365-8711.2000.03832.x.
- M. Colless, G. Dalton, S. Maddox, W. Sutherland, P. Norberg, S. Cole, J. Bland-Hawthorn, T. Bridges, R. Cannon, C. Collins, W. Couch, N. Cross, K. Deeley, R. De Propriis, S. P. Driver, G. Efstathiou, R. S. Ellis, C. S. Frenk, K. Glazebrook, C. Jackson, O. Lahav, I. Lewis, S. Lumsden, D. Madgwick, J. A. Peacock, B. A. Peterson, I. Price, M. Seaborne, and K. Taylor. The 2dF Galaxy Redshift Survey: spectra and redshifts. *MNRAS*, 328(4):1039–1063, Dec. 2001. doi: 10.1046/j.1365-8711.2001.04902.x.
- M. C. Cooper, J. A. Newman, B. J. Weiner, R. Yan, C. N. A. Willmer, K. Bundy, A. L. Coil, C. J. Conselice, M. Davis, S. M. Faber, B. F. Gerke, P. Guhathakurta, D. C. Koo, and K. G. Noeske. The DEEP2 Galaxy Redshift Survey: the role of galaxy environment in the cosmic star formation history. *MNRAS*, 383(3):1058–1078, Jan. 2008. doi: 10.1111/j.1365-2966.2007.12613.x.
- O. Cucciati, B. C. Lemaux, G. Zamorani, O. Le Fèvre, L. A. M. Tasca, N. P. Hathi, K. G. Lee, S. Bardelli, P. Cassata, B. Garilli, V. Le Brun, D. Maccagni, L. Pentericci, R. Thomas, E. Vanzella, E. Zucca, L. M. Lubin, R. Amorin, L. P. Cassarà, A. Cimatti, M. Talia, D. Vergani, A. Koekemoer, J. Pforr, and M. Salvato. The progeny of a cosmic titan: a massive multi-component proto-supercluster in formation at  $z = 2.45$  in VUDS. *A&A*, 619:A49, Nov. 2018. doi: 10.1051/0004-6361/201833655.
- B. Darvish, B. Mobasher, D. Sobral, N. Scoville, and M. Aragon-Calvo. A Comparative Study of Density

- Field Estimation for Galaxies: New Insights into the Evolution of Galaxies with Environment in COSMOS out to  $z \sim 3$ . *ApJ*, 805(2):121, June 2015. doi: 10.1088/0004-637X/805/2/121.
- B. Darvish, B. Mobasher, D. Sobral, A. Rettura, N. Scoville, A. Faisst, and P. Capak. The Effects of the Local Environment and Stellar Mass on Galaxy Quenching to  $z \sim 3$ . *ApJ*, 825(2):113, July 2016. doi: 10.3847/0004-637X/825/2/113.
- M. Davis, S. M. Faber, J. Newman, A. C. Phillips, R. S. Ellis, C. C. Steidel, C. Conselice, A. L. Coil, D. P. Finkbeiner, D. C. Koo, P. Guhathakurta, B. Weiner, R. Schiavon, C. Willmer, N. Kaiser, G. A. Luppino, G. Wirth, A. Connolly, P. Eisenhardt, M. Cooper, and B. Gerke. Science Objectives and Early Results of the DEEP2 Redshift Survey. In P. Guhathakurta, editor, *Discoveries and Research Prospects from 6- to 10-Meter-Class Telescopes II*, volume 4834 of *Society of Photo-Optical Instrumentation Engineers (SPIE) Conference Series*, pages 161–172, Feb. 2003. doi: 10.1117/12.457897.
- K. Dolag. Simulating large-scale structure formation with magnetic fields. *Astronomische Nachrichten*, 327: 575, June 2006. doi: 10.1002/asna.200610595.
- A. Dressler. Galaxy morphology in rich clusters: implications for the formation and evolution of galaxies. *ApJ*, 236:351–365, Mar. 1980. doi: 10.1086/157753.
- M. Einasto, E. Tago, J. Jaaniste, J. Einasto, and H. Andernach. The supercluster-void network I. The supercluster catalogue and large-scale distribution. *A&AS*, 123:119–133, May 1997. doi: 10.1051/aas:1997340.
- V. R. Eke, J. F. Navarro, and C. S. Frenk. The Evolution of X-Ray Clusters in a Low-Density Universe. *ApJ*, 503(2):569–592, Aug. 1998. doi: 10.1086/306008.
- D. Elbaz, E. Daddi, D. Le Borgne, M. Dickinson, D. M. Alexander, R. R. Chary, J. L. Starck, W. N. Brandt, M. Kitzbichler, E. MacDonald, M. Nonino, P. Popesso, D. Stern, and E. Vanzella. The reversal of the star formation-density relation in the distant universe. *A&A*, 468(1):33–48, June 2007. doi: 10.1051/0004-6361:20077525.
- A. E. Evrard, T. J. MacFarland, H. M. P. Couchman, J. M. Colberg, N. Yoshida, S. D. M. White, A. Jenkins, C. S. Frenk, F. R. Pearce, J. A. Peacock, and P. A. Thomas. Galaxy Clusters in Hubble Volume Simulations: Cosmological Constraints from Sky Survey Populations. *ApJ*, 573(1):7–36, July 2002. doi: 10.1086/340551.
- S. M. Faber, A. C. Phillips, R. I. Kibrick, B. Alcott, S. L. Allen, J. Burrous, T. Cantrall, D. Clarke, A. L. Coil, D. J. Cowley, M. Davis, W. T. S. Deich, K. Dietsch, D. K. Gilmore, C. A. Harper, D. F. Hilyard, J. P. Lewis, M. McVeigh, J. Newman, J. Osborne, R. Schiavon, R. J. Stover, D. Tucker, V. Wallace, M. Wei, G. Wirth, and C. A. Wright. The DEIMOS spectrograph for the Keck II Telescope: integration and testing. In M. Iye and A. F. M. Moorwood, editors, *Instrument Design and Performance for Optical/Infrared Ground-based Telescopes*, volume 4841 of *Society of Photo-Optical Instrumentation Engineers (SPIE) Conference Series*, pages 1657–1669, Mar. 2003. doi: 10.1117/12.460346.
- C. S. Frenk, A. E. Evrard, S. D. M. White, and F. J. Summers. Galaxy Dynamics in Clusters. *ApJ*, 472: 460, Dec. 1996. doi: 10.1086/178079.
- R. R. Gal, B. C. Lemaux, L. M. Lubin, D. Kocevski, and G. K. Squires. The Complex Structure of the Cl 1604 Supercluster at  $z \sim 0.9$ . *ApJ*, 684(2):933–956, Sept. 2008. doi: 10.1086/590416.
- M. J. Geller and J. P. Huchra. Mapping the Universe. *Science*, 246(4932):897–903, Nov. 1989. doi: 10.1126/science.246.4932.897.
- S. P. D. Gill, A. Knebe, and B. K. Gibson. The evolution of substructure - III. The outskirts of clusters. *MNRAS*, 356(4):1327–1332, Feb. 2005. doi: 10.1111/j.1365-2966.2004.08562.x.
- I. M. Gioia, J. P. Henry, C. R. Mullis, H. Ebeling, and A. Wolter. RX J1716.6+6708: A Young Cluster at  $Z=0.81$ . *AJ*, 117(6):2608–2616, June 1999. doi: 10.1086/300868.
- I. M. Gioia, J. P. Henry, C. R. Mullis, H. Böhringer, U. G. Briel, W. Voges, and J. P. Huchra. The ROSAT North Ecliptic Pole Survey: the Optical Identifications. *ApJS*, 149(1):29–51, Nov. 2003. doi: 10.1086/378229.
- M. D. Gladders and H. K. C. Yee. The Red-Sequence Cluster Survey. I. The Survey and Cluster Catalogs for Patches RCS 0926+37 and RCS 1327+29. *ApJS*, 157(1):1–29, Mar. 2005. doi: 10.1086/427327.
- P. L. Gómez, R. C. Nichol, C. J. Miller, M. L. Balogh, T. Goto, A. I. Zabludoff, A. K. Romer, M. Bernardi,



- R. Sheth, A. M. Hopkins, F. J. Castander, A. J. Connolly, D. P. Schneider, J. Brinkmann, D. Q. Lamb, M. SubbaRao, and D. G. York. Galaxy Star Formation as a Function of Environment in the Early Data Release of the Sloan Digital Sky Survey. *ApJ*, 584(1):210–227, Feb. 2003. doi: 10.1086/345593.
- R. Grützbauch, C. J. Conselice, A. E. Bauer, A. F. L. Bluck, R. W. Chuter, F. Buitrago, A. Mortlock, T. Weinzierl, and S. Jogee. The relationship between star formation rates, local density and stellar mass up to  $z \sim 3$  in the GOODS NICMOS Survey. *MNRAS*, 418(2):938–948, Dec. 2011. doi: 10.1111/j.1365-2966.2011.19559.x.
- J. E. Gunn and I. Gott, J. Richard. On the Infall of Matter Into Clusters of Galaxies and Some Effects on Their Evolution. *ApJ*, 176:1, Aug. 1972. doi: 10.1086/151605.
- H. Guo, M. G. Jones, J. Wang, and L. Lin. Star Formation and Quenching of Central Galaxies from Stacked HI Measurements. *arXiv e-prints*, art. arXiv:2105.13505, May 2021.
- C. P. Haines, M. J. Pereira, A. J. R. Sanderson, G. P. Smith, E. Egami, A. Babul, A. C. Edge, A. Finoguenov, S. M. Moran, and N. Okabe. LoCuSS: A Dynamical Analysis of X-Ray Active Galactic Nuclei in Local Clusters. *ApJ*, 754(2):97, Aug. 2012. doi: 10.1088/0004-637X/754/2/97.
- Y. Hashimoto, J. P. Henry, G. Hasinger, G. Szokoly, and M. Schmidt. Galaxy populations of double cluster RX J1053.7+5735 at  $z = 1.13$ . *A&A*, 439(1):29–33, Aug. 2005. doi: 10.1051/0004-6361:20042112.
- J. P. Henry, C. R. Mullis, W. Voges, H. Böhringer, U. G. Briel, I. M. Gioia, and J. P. Huchra. The ROSAT North Ecliptic Pole Survey: The X-Ray Catalog. *ApJS*, 162(2):304–328, Feb. 2006. doi: 10.1086/498749.
- J. A. Hester. Ram Pressure Stripping in Clusters and Groups. *ApJ*, 647(2):910–921, Aug. 2006. doi: 10.1086/505614.
- D. W. Hogg, M. R. Blanton, J. Brinchmann, D. J. Eisenstein, D. J. Schlegel, J. E. Gunn, T. A. McKay, H.-W. Rix, N. A. Bahcall, J. Brinkmann, and A. Meiksin. The Dependence on Environment of the Color-Magnitude Relation of Galaxies. *ApJ*, 601(1):L29–L32, Jan. 2004. doi: 10.1086/381749.
- D. Hung, B. C. Lemaux, R. R. Gal, A. R. Tomczak, L. M. Lubin, O. Cucciati, D. Pelliccia, L. Shen, O. Le Fèvre, P. F. Wu, D. D. Kocevski, S. Mei, and G. K. Squires. Establishing a new technique for discovering large-scale structure using the ORELSE survey. *MNRAS*, 491(4):5524–5554, Feb. 2020. doi: 10.1093/mnras/stz3164.
- G. Kauffmann, S. D. M. White, T. M. Heckman, B. Ménard, J. Brinchmann, S. Charlot, C. Tremonti, and J. Brinkmann. The environmental dependence of the relations between stellar mass, structure, star formation and nuclear activity in galaxies. *MNRAS*, 353(3):713–731, Sept. 2004. doi: 10.1111/j.1365-2966.2004.08117.x.
- A. M. Koekemoer, H. Aussel, D. Calzetti, P. Capak, M. Giavalisco, J. P. Kneib, A. Leauthaud, O. Le Fèvre, H. J. McCracken, R. Massey, B. Mobasher, J. Rhodes, N. Scoville, and P. L. Shopbell. The COSMOS Survey: Hubble Space Telescope Advanced Camera for Surveys Observations and Data Processing. *ApJS*, 172(1):196–202, Sept. 2007. doi: 10.1086/520086.
- B. C. Lemaux, L. M. Lubin, A. Shapley, D. Kocevski, R. R. Gal, and G. K. Squires. The Origin of [O II] in Post-starburst and Red-sequence Galaxies in High-redshift Clusters. *ApJ*, 716(2):970–992, June 2010. doi: 10.1088/0004-637X/716/2/970.
- B. C. Lemaux, E. Le Floc’h, O. Le Fèvre, O. Ilbert, L. Tresse, L. M. Lubin, G. Zamorani, R. R. Gal, P. Ciliegi, P. Cassata, D. D. Kocevski, E. J. McGrath, S. Bardelli, E. Zucca, and G. K. Squires. Hidden starbursts and active galactic nuclei at  $0 < z < 4$  from the Herschel-VVDS-CFHTLS-D1 field: Inferences on coevolution and feedback. *A&A*, 572:A90, Dec. 2014. doi: 10.1051/0004-6361/201323089.
- B. C. Lemaux, A. R. Tomczak, L. M. Lubin, P. F. Wu, R. R. Gal, N. Rumbaugh, D. D. Kocevski, and G. K. Squires. Chronos and KAIROS: MOSFIRE observations of post-starburst galaxies in  $z \sim 1$  clusters and groups. *MNRAS*, 472(1):419–438, Nov. 2017. doi: 10.1093/mnras/stx1579.
- B. C. Lemaux, A. R. Tomczak, L. M. Lubin, R. R. Gal, L. Shen, D. Pelliccia, P. F. Wu, D. Hung, S. Mei, O. Le Fèvre, N. Rumbaugh, D. D. Kocevski, and G. K. Squires. Persistence of the colour-density relation and efficient environmental quenching to  $z \sim 1.4$ . *MNRAS*, 490(1):1231–1254, Nov. 2019. doi: 10.1093/mnras/stz2661.
- I. Lewis, M. Balogh, R. De Propris, W. Couch, R. Bower, A. Offer, J. Bland-Hawthorn, I. K. Baldry, C. Baugh, T. Bridges, R. Cannon, S. Cole, M. Colless, C. Collins, N. Cross, G. Dalton, S. P. Driver,

- G. Efstathiou, R. S. Ellis, C. S. Frenk, K. Glazebrook, E. Hawkins, C. Jackson, O. Lahav, S. Lumsden, S. Maddox, D. Madgwick, P. Norberg, J. A. Peacock, W. Percival, B. A. Peterson, W. Sutherland, and K. Taylor. The 2dF Galaxy Redshift Survey: the environmental dependence of galaxy star formation rates near clusters. *MNRAS*, 334(3):673–683, Aug. 2002. doi: 10.1046/j.1365-8711.2002.05558.x.
- L. M. Lubin, R. R. Gal, B. C. Lemaux, D. D. Kocevski, and G. K. Squires. The Observations of Redshift Evolution in Large-Scale Environments (ORELSE) Survey. I. The Survey Design and First Results on CL 0023+0423 at  $z = 0.84$  and RX J1821.6+6827 at  $z = 0.82$ . *AJ*, 137(6):4867–4883, June 2009. doi: 10.1088/0004-6256/137/6/4867.
- B. J. Maughan, L. R. Jones, H. Ebeling, and C. Scharf. The evolution of the cluster X-ray scaling relations in the Wide Angle ROSAT Pointed Survey sample at  $0.6 < z < 1.0$ . *MNRAS*, 365(2):509–529, Jan. 2006. doi: 10.1111/j.1365-2966.2005.09717.x.
- E. Merlin, A. Fontana, H. C. Ferguson, J. S. Dunlop, D. Elbaz, N. Bourne, V. A. Bruce, F. Buitrago, M. Castellano, C. Schreiber, A. Grazian, R. J. McLure, K. Okumura, X. Shu, T. Wang, R. Amorín, K. Boutsia, N. Cappelluti, A. Comastri, S. Derriere, S. M. Faber, and P. Santini. T-PHOT: A new code for PSF-matched, prior-based, multiwavelength extragalactic deconvolution photometry. *A&A*, 582:A15, Oct. 2015. doi: 10.1051/0004-6361/201526471.
- S. Miyazaki, Y. Komiyama, M. Sekiguchi, S. Okamura, M. Doi, H. Furusawa, M. Hamabe, K. Imi, M. Kimura, F. Nakata, N. Okada, M. Ouchi, K. Shimasaku, M. Yagi, and N. Yasuda. Subaru Prime Focus Camera – Suprime-Cam. *PASJ*, 54:833–853, Dec. 2002. doi: 10.1093/pasj/54.6.833.
- B. Moore, N. Katz, G. Lake, A. Dressler, and A. Oemler. Galaxy harassment and the evolution of clusters of galaxies. *Nature*, 379(6566):613–616, Feb. 1996. doi: 10.1038/379613a0.
- B. Moore, G. Lake, and N. Katz. Morphological Transformation from Galaxy Harassment. *ApJ*, 495(1):139–151, Mar. 1998. doi: 10.1086/305264.
- J. Moustakas, J. Kennicutt, Robert C., and C. A. Tremonti. Optical Star Formation Rate Indicators. *ApJ*, 642(2):775–796, May 2006. doi: 10.1086/500964.
- A. Muzzin, G. Wilson, H. K. C. Yee, D. Gilbank, H. Hoekstra, R. Demarco, M. Balogh, P. van Dokkum, M. Franx, E. Ellingson, A. Hicks, J. Nantais, A. Noble, M. Lacy, C. Lidman, A. Rettura, J. Surace, and T. Webb. The Gemini Cluster Astrophysics Spectroscopic Survey (GCLASS): The Role of Environment and Self-regulation in Galaxy Evolution at  $z \sim 1$ . *ApJ*, 746(2):188, Feb. 2012. doi: 10.1088/0004-637X/746/2/188.
- A. Muzzin, R. F. J. van der Burg, S. L. McGee, M. Balogh, M. Franx, H. Hoekstra, M. J. Hudson, A. Noble, D. S. Taranu, T. Webb, G. Wilson, and H. K. C. Yee. The Phase Space and Stellar Populations of Cluster Galaxies at  $z \sim 1$ : Simultaneous Constraints on the Location and Timescale of Satellite Quenching. *ApJ*, 796(1):65, Nov. 2014. doi: 10.1088/0004-637X/796/1/65.
- A. G. Noble, T. M. A. Webb, A. Muzzin, G. Wilson, H. K. C. Yee, and R. F. J. van der Burg. A Kinematic Approach to Assessing Environmental Effects: Star-forming Galaxies in a  $z \sim 0.9$  SpARCS Cluster Using Spitzer 24  $\mu\text{m}$  Observations. *ApJ*, 768(2):118, May 2013. doi: 10.1088/0004-637X/768/2/118.
- G. Noirot, D. Stern, S. Mei, D. Wylezalek, E. A. Cooke, C. De Breuck, A. Galametz, N. A. Hatch, J. Vernet, M. Brodwin, P. Eisenhardt, A. H. Gonzalez, M. Jarvis, A. Rettura, N. Seymour, and S. A. Stanford. HST Grism Confirmation of 16 Structures at  $1.4 < z < 2.8$  from the Clusters Around Radio-Loud AGN (CARLA) Survey. *ApJ*, 859(1):38, May 2018. doi: 10.3847/1538-4357/aabadb.
- J. B. Oke, M. Postman, and L. M. Lubin. A Study of Nine High-Redshift Clusters of Galaxies. I. The Survey. *AJ*, 116(2):549–559, Aug. 1998. doi: 10.1086/300462.
- L. J. Old, M. L. Balogh, R. F. J. van der Burg, A. Biviano, H. K. C. Yee, I. Pintos-Castro, K. Webb, A. Muzzin, G. Rudnick, B. Vulcani, B. Poggianti, M. Cooper, D. Zaritsky, P. Cerulo, G. Wilson, J. C. C. Chan, C. Lidman, S. McGee, R. Demarco, B. Forrest, G. De Lucia, D. Gilbank, E. Kukstas, I. G. McCarthy, P. Jablonka, J. Nantais, A. Noble, A. M. M. Reeves, and H. Shipley. The GOGREEN survey: the environmental dependence of the star-forming galaxy main sequence at  $1.0 < z < 1.5$ . *MNRAS*, 493(4):5987–6000, Apr. 2020. doi: 10.1093/mnras/staa579.
- S. G. Patel, D. D. Kelson, B. P. Holden, M. Franx, and G. D. Illingworth. The Star-formation-rate-Density Relation at  $0.6 < z < 0.9$  and the Role of Star-forming Galaxies. *ApJ*, 735(1):53, July 2011. doi:

10.1088/0004-637X/735/1/53.

- D. Pelliccia, B. C. Lemaux, A. R. Tomczak, L. M. Lubin, L. Shen, B. Epinat, P.-F. Wu, R. R. Gal, N. Rumbaugh, D. D. Kocevski, L. Tresse, and G. Squires. Searching for environmental effects on galaxy kinematics in groups and clusters at  $z \sim 1$  from the ORELSE survey. *MNRAS*, 482(3):3514–3549, Jan. 2019. doi: 10.1093/mnras/sty2876.
- M. Pierre, F. Pacaud, P. A. Duc, J. P. Willis, S. Andreon, I. Valtchanov, B. Altieri, G. Galaz, A. Gueguen, J. P. Le Fèvre, O. Le Fèvre, T. Ponman, P. G. Sprimont, J. Surdej, C. Adami, A. Alshino, M. Bremer, L. Chiappetti, A. Detal, O. Garcet, E. Gosset, C. Jean, D. Maccagni, C. Marinoni, A. Mazure, H. Quintana, and A. Read. The XMM Large-Scale Structure survey: a well-controlled X-ray cluster sample over the D1 CFHTLS area. *MNRAS*, 372(2):591–608, Oct. 2006. doi: 10.1111/j.1365-2966.2006.10886.x.
- P. Popesso, G. Rodighiero, A. Saintonge, P. Santini, A. Grazian, D. Lutz, M. Brusa, B. Altieri, P. Andreani, H. Aussel, S. Berta, A. Bongiovanni, A. Cava, J. Cepa, A. Cimatti, E. Daddi, H. Dominguez, D. Elbaz, N. Förster Schreiber, R. Genzel, C. Gruppioni, G. Magdis, R. Maiolino, B. Magnelli, R. Nordon, A. M. Pérez García, A. Poglitsch, F. Pozzi, L. Riguccini, M. Sanchez-Portal, L. Shao, E. Sturm, L. Tacconi, I. Valtchanov, E. Wieprecht, and M. Wetzstein. The effect of environment on star forming galaxies at redshift. I. First insight from PACS. *A&A*, 532:A145, Aug. 2011. doi: 10.1051/0004-6361/201015672.
- J. Rasmussen, J. S. Mulchaey, L. Bai, T. J. Ponman, S. Raychaudhury, and A. Dariush. The Suppression of Star Formation and the Effect of the Galaxy Environment in Low-redshift Galaxy Groups. *ApJ*, 757(2):122, Oct. 2012. doi: 10.1088/0004-637X/757/2/122.
- P. Rosati, R. Della Ceca, C. Norman, and R. Giacconi. The ROSAT Deep Cluster Survey: The X-Ray Luminosity Function out to  $z = 0.8$ . *ApJ*, 492(1):L21–L24, Jan. 1998. doi: 10.1086/311085.
- N. Rumbaugh, B. C. Lemaux, A. Tomczak, D. D. Kocevski, L. M. Lubin, P. F. Wu, R. R. Gal, L. Shen, A. Mansheim, C. D. Fassnacht, and G. K. Squires. X-ray-emitting active galactic nuclei from  $z = 0.6$  to 1.3 in the intermediate- and high-density environments of the ORELSE survey. *MNRAS*, 466(1):496–519, Apr. 2017. doi: 10.1093/mnras/stw3091.
- J. S. Santos, B. Altieri, I. Valtchanov, A. Nastasi, H. Bohringer, G. Cresci, D. Elbaz, R. Fassbender, P. Rosati, P. Tozzi, and M. Verdugo. The reversal of the SF-density relation in a massive, X-ray-selected galaxy cluster at  $z = 1.58$ : results from Herschel. *MNRAS*, 447:L65–L69, Feb. 2015. doi: 10.1093/mnrasl/slu180.
- N. Scoville, H. Aussel, M. Brusa, P. Capak, C. M. Carollo, M. Elvis, M. Giavalisco, L. Guzzo, G. Hasinger, C. Impey, J. P. Kneib, O. LeFevre, S. J. Lilly, B. Mobasher, A. Renzini, R. M. Rich, D. B. Sanders, E. Schinnerer, D. Schminovich, P. Shopbell, Y. Taniguchi, and N. D. Tyson. The Cosmic Evolution Survey (COSMOS): Overview. *ApJS*, 172(1):1–8, Sept. 2007. doi: 10.1086/516585.
- L. Shen, N. A. Miller, B. C. Lemaux, A. R. Tomczak, L. M. Lubin, N. Rumbaugh, C. D. Fassnacht, R. H. Becker, R. R. Gal, P.-F. Wu, and G. Squires. The properties of radio galaxies and the effect of environment in large-scale structures at  $z \sim 1$ . *MNRAS*, 472(1):998–1022, Nov. 2017. doi: 10.1093/mnras/stx1984.
- L. Shen, A. R. Tomczak, B. C. Lemaux, D. Pelliccia, L. M. Lubin, N. A. Miller, S. Perrotta, C. D. Fassnacht, R. H. Becker, R. R. Gal, P.-F. Wu, and G. Squires. Possible evidence of the radio AGN quenching of neighbouring galaxies at  $z \sim 1$ . *MNRAS*, 484(2):2433–2446, Apr. 2019. doi: 10.1093/mnras/stz152.
- R. A. Simcoe, M. R. Metzger, T. A. Small, and G. Araya. LFC - A New Wide-Field Imager at Palomar. In *American Astronomical Society Meeting Abstracts #196*, volume 196 of *American Astronomical Society Meeting Abstracts*, page 52.09, May 2000.
- R. J. Smith, M. J. Hudson, J. R. Lucey, J. E. Nelán, and G. A. Wegner. The NOAO Fundamental Plane Survey - III. Variations in the stellar populations of red-sequence galaxies from the cluster core to the virial radius. *MNRAS*, 369(3):1419–1436, July 2006. doi: 10.1111/j.1365-2966.2006.10393.x.
- S. A. Stanford, B. Holden, P. Rosati, P. R. Eisenhardt, D. Stern, G. Squires, and H. Spinrad. An X-Ray-Selected Galaxy Cluster at  $z=1.11$  in the ROSAT Deep Cluster Survey. *AJ*, 123(2):619–626, Feb. 2002. doi: 10.1086/338442.
- C. M. S. Straatman, L. R. Spitler, R. F. Quadri, I. Labbé, K. Glazebrook, S. E. Persson, C. Papovich, K.-V. H. Tran, G. B. Brammer, M. Cowley, A. Tomczak, T. Nanayakkara, L. Alcorn, R. Allen, A. Broussard, P. van Dokkum, B. Forrest, J. van Houdt, G. G. Kacprzak, L. Kavinwanichakij, D. D. Kelson, J. Lee, P. J.

- McCarthy, N. Mehrrens, A. Monson, D. Murphy, G. Rees, V. Tilvi, and K. E. Whitaker. The FourStar Galaxy Evolution Survey (ZFOURGE): Ultraviolet to Far-infrared Catalogs, Medium-bandwidth Photometric Redshifts with Improved Accuracy, Stellar Masses, and Confirmation of Quiescent Galaxies to  $z \sim 3.5$ . *ApJ*, 830(1):51, Oct. 2016. doi: 10.3847/0004-637X/830/1/51.
- V. Strazzullo, R. Gobat, E. Daddi, M. Onodera, M. Carollo, M. Dickinson, A. Renzini, N. Arimoto, A. Cimatti, A. Finoguenov, and R. R. Chary. Galaxy Evolution in Overdense Environments at High Redshift: Passive Early-type Galaxies in a Cluster at  $z \sim 2$ . *ApJ*, 772(2):118, Aug. 2013. doi: 10.1088/0004-637X/772/2/118.
- A. R. Tomczak, B. C. Lemaux, L. M. Lubin, R. R. Gal, P.-F. Wu, B. Holden, D. D. Kocevski, S. Mei, D. Pelliccia, N. Rumbaugh, and L. Shen. Glimpsing the imprint of local environment on the galaxy stellar mass function. *MNRAS*, 472(3):3512–3531, Dec. 2017. doi: 10.1093/mnras/stx2245.
- A. R. Tomczak, B. C. Lemaux, L. M. Lubin, D. Pelliccia, L. Shen, R. R. Gal, D. Hung, D. D. Kocevski, O. Le Fèvre, S. Mei, N. Rumbaugh, G. K. Squires, and P.-F. Wu. Conditional quenching: a detailed look at the SFR-density relation at  $z \sim 0.9$  from ORELSE. *MNRAS*, 484(4):4695–4710, Apr. 2019. doi: 10.1093/mnras/stz342.
- K.-V. H. Tran, C. Papovich, A. Saintonge, M. Brodwin, J. S. Dunlop, D. Farrah, K. D. Finkelstein, S. L. Finkelstein, J. Lotz, R. J. McLure, I. Momcheva, and C. N. A. Willmer. Reversal of Fortune: Confirmation of an Increasing Star Formation-Density Relation in a Cluster at  $z = 1.62$ . *ApJ*, 719(2):L126–L129, Aug. 2010. doi: 10.1088/2041-8205/719/2/L126.
- A. Vikhlinin, B. R. McNamara, W. Forman, C. Jones, H. Quintana, and A. Hornstrup. Evolution of Cluster X-Ray Luminosities and Radii: Results from the 160 Square Degree ROSAT Survey. *ApJ*, 498(1):L21–L25, May 1998. doi: 10.1086/311305.
- T. Wang, D. Elbaz, E. Daddi, A. Finoguenov, D. Liu, C. Schreiber, S. Martín, V. Strazzullo, F. Valentino, R. van der Burg, A. Zanella, L. Ciesla, R. Gobat, A. Le Brun, M. Pannella, M. Sargent, X. Shu, Q. Tan, N. Cappelluti, and Y. Li. Discovery of a Galaxy Cluster with a Violently Starbursting Core at  $z = 2.506$ . *ApJ*, 828(1):56, Sept. 2016. doi: 10.3847/0004-637X/828/1/56.
- B. J. Weiner, C. Papovich, K. Bundy, C. J. Conselice, M. C. Cooper, R. S. Ellis, R. J. Ivison, K. G. Noeske, A. C. Phillips, and R. Yan. AEGIS: Extinction and Star Formation Tracers from Line Emission. *ApJ*, 660(1):L39–L42, May 2007. doi: 10.1086/517925.
- S. Wuyts, I. Labbé, N. M. Förster Schreiber, M. Franx, G. Rudnick, G. B. Brammer, and P. G. van Dokkum. FIREWORKS  $U_{38}$ -to- $24 \mu\text{m}$  Photometry of the GOODS Chandra Deep Field-South: Multiwavelength Catalog and Total Infrared Properties of Distant  $K_s$ -selected Galaxies. *ApJ*, 682(2):985–1003, Aug. 2008. doi: 10.1086/588749.
- S. Wuyts, N. M. Förster Schreiber, E. J. Nelson, P. G. van Dokkum, G. Brammer, Y.-Y. Chang, S. M. Faber, H. C. Ferguson, M. Franx, M. Fumagalli, R. Genzel, N. A. Grogin, D. D. Kocevski, A. M. Koekemoer, B. Lundgren, D. Lutz, E. J. McGrath, I. Momcheva, D. Rosario, R. E. Skelton, L. J. Tacconi, A. van der Wel, and K. E. Whitaker. A CANDELS-3D-HST synergy: Resolved Star Formation Patterns at  $0.7 < z < 1.5$ . *ApJ*, 779(2):135, Dec. 2013. doi: 10.1088/0004-637X/779/2/135.
- F. Ziparo, P. Popesso, A. Finoguenov, A. Biviano, S. Wuyts, D. Wilman, M. Salvato, M. Tanaka, K. Nandra, D. Lutz, D. Elbaz, M. Dickinson, B. Altieri, H. Aussel, S. Berta, A. Cimatti, D. Fadda, R. Genzel, E. Le Floc’h, B. Magnelli, R. Nordon, A. Poglitsch, F. Pozzi, M. S. Portal, L. Tacconi, F. E. Bauer, W. N. Brandt, N. Cappelluti, M. C. Cooper, and J. S. Mulchaey. Reversal or no reversal: the evolution of the star formation rate-density relation up to  $z \sim 1.6$ . *MNRAS*, 437(1):458–474, Jan. 2014. doi: 10.1093/mnras/stt1901.

## 712 **Appendix**

713 Much of my first two weeks was spent collating data from various files within the ORELSE  
714 survey data. Matching objects through their spectroscopic and photometric IDs, I was able  
715 to combine data that covered SFR UVIR, SFR OII, SED fitted SFR, redshift, mask/slit  
716 information, associated parent structure, and much more into 15 files (1 for each field in  
717 ORELSE) which totaled to more than 1.5 million possible objects (though a most of those  
718 possible were not).